Spring 4-23-2010

Classification, Synthesis and Characterization of Pyridyl Porphyrin Frameworks

Lucas D. DeVries
University of Nebraska at Lincoln, lucas.d.devries@gmail.com

CLASSIFICATION, SYNTHESIS AND CHARACTERIZATION OF PYRIDYL PORPHYRIN FRAMEWORKS

by

Lucas D. DeVries

A THESIS

Presented to the Faculty of

The Graduate College at the University of Nebraska

In Partial Fulfillment of Requirements

For the Degree of Master of Science

Major: Chemistry

Under the Supervision of Professor Wonyoung Choe

Lincoln, Nebraska

April, 2010

CLASSIFICATION, SYNTHESIS AND CHARACTERIZATION OF PYRIDYL PORPHYRIN FRAMEWORKS

Lucas D. DeVries, M.S.

University of Nebraska, 2010

Adviser: Wonyoung Choe

Structural analysis of a solid-state material is vital because the structure often determines the physical (or chemical) properties of the material. An understanding of the relationship between structural components and bulk properties can be used to design materials with specific properties. To achieve such understanding, two things are required: a rigorous structural analysis method and a study of the properties of materials with noteworthy structural features.

In this thesis, the author reviews 44 pyridyl porphyrin frameworks in an effort to determine how these framework structures are formed, and if any overreaching trends can be observed. The observed trends are used to develop a method to analyze pyridyl porphyrin frameworks based on the types of porphyrins used, the metal node used, and the metal-to-porphyrin ratio. The structures of two new frameworks (MPF-3 and E-MOF-1) are also analyzed and tested for their structural flexibility. The structural features of each framework are correlated to the property being examined (flexibility). The type of flexibility demonstrated is strongly related to the structure of the individual framework. The structural analysis of the frameworks presented here is a small but significant step towards the rational design of flexible metal-organic frameworks.

ACKNOWLEDGEMENTS

I would like to thank the University of Nebraska-Lincoln Chemistry Department for the opportunity to explore and grow my chemistry career here at UNL. I have enjoyed my time here with the professors, students, and group members I have met. I am where I am today because of their influence.

I could not have completed this work without the aid of several important people. I would like to thank Eun-Young Choi and Evan Hurley for the experiments that became two of my projects, Chunhua Hu for his single-crystal diffraction work, and Matthew Suchomel at Argonne National Labs for his expertise in synchrotron powder diffraction data.

None of this would have been possible without the knowledge, support, and enthusiasm of Professor Wonyoung Choe and everyone in the Choe lab. I have gained so much personally and professionally from my discussions and experiences with this fine group of people. I feel grateful to have been allowed to be part of it.

I would like to thank my sister for her good humor and my mother and my father for their encouragement as I seek to find the right career, the right path for myself. As I leave UNL, I know what I have gained here will set my feet on that path.

TABLE OF CONTENTS

APPENDIX 2 Calculations for the Cell Parameters, Flexible Model, and Coefficient of Thermal Expansion

CHAPTER 1

METAL-ORGANIC FRAMEWORKS: TOPOLOGY AND FLEXIBILITY

1.1 Introduction

The following thesis contains a new classification system for coordination polymers[1] formed of derivatives of tetrapyridylporphyrin building units, and reports two new flexible frameworks[2] whose properties have been characterized.

1.2 Coordination Polymers and Metal-Organic Frameworks

Over 300 years ago a new pigment soon to be known as Prussian Blue was discovered in Berlin.[1] Many years later, this pigment was characterized and found to be the world's first man-made coordination polymer.[1] A coordination polymer contains two basic units: a metal node (or metal complex) with usually well-defined coordination geometry and a coordinating ligand.[1] The coordination polymer is also defined as a molecular framework extending infinitely in at least one direction.[1] Coordination polymers must also be formed of coordination bonds because hydrogen bonding of a similar nature does not qualify a material as a coordination polymer.[1] These materials are interesting due to the degree of control made possible by the choice of metal coordination geometry and ligand shape (Figure 1.1). The ratio of metal nodes to ligand can also influence the final structure.[3]

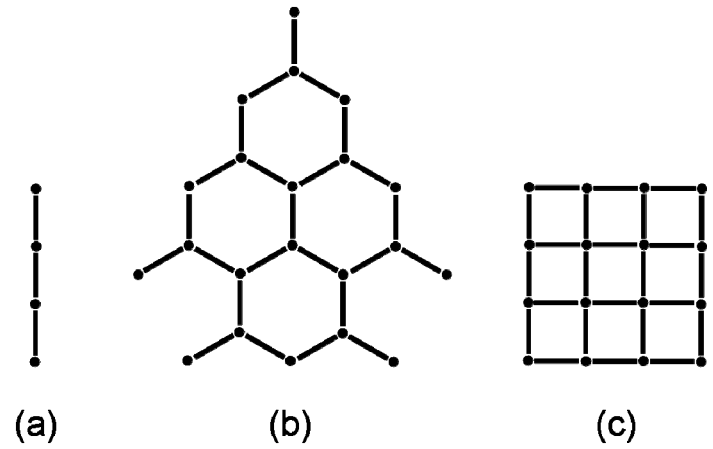

Figure 1.1. Influence of metal node coordination geometry and ligand shape on the final structure. The circles represent metal nodes and the lines are coordination ligands. All of the ligands are linear and the coordination number of the metal nodes is (a) 2, (b) 3, and (c) 4, forming 1D (a) and 2D nets (b,c).

The terms coordination polymer and metal-organic framework (MOF) have been debated recently.[4] Some argue that a coordination polymer is different from a MOF due to bond strength and differing building units.[4c] Others would say that the dimensionality of the structure is what determines if it should be labeled a coordination polymer or MOF.[4a] This debate is ongoing and no consensus has been reached at present. For the purposes of this thesis, the terms coordination polymer and MOF will be used interchangeably.

1.3 Flexible Frameworks

The importance of structural control is demonstrated by a new type of metal-organic framework (MOF), flexible frameworks, that can undergo a reversible structural transformation in response to a change in temperature, pressure, or guest removal/uptake.[2,5-7] Flexible frameworks have been reported that can separate molecules

by size, accommodate various guest molecules, and have demonstrated variable magnetic properties. [2,5-7] The specific topology and structure of a framework can determine if it is possible for the framework to flex. [2,5-7] Analyzing and understanding flexible frameworks provides insight into how to design future frameworks to be flexible. Using this knowledge could lead to the design of flexible frameworks with the properties described above, or exciting new properties not yet observed.

1.4 Organization of Thesis

Chapter 1 introduces the basic definitions of the types of materials discussed in this thesis. Chapter 2 presents a review of the dimensionality of pyridyl porphyrin frameworks.[3] This review was originally published in the *Journal of Chemical Crystallography*.[3] A search of the Cambridge Structural Database and a literature search was conducted, by the author, who also created all figures for the article from published single-crystal data.

Chapter 3 describes a 2D flexible framework that is sensitive to guest uptake and removal.[8] The data in Chapter 3 was originally published in *Crystal Growth and Design*.[8] The initial synthesis and the synthesis of a single-crystal quality sample were developed by Eun-Young Choi with the aid of Richard Novotny. Eun-Young Choi also performed the initial solvent experiments on MPF-3. The single-crystal data were resolved by Chunhua Hu. The author conducted the solvation experiments, analysis of the powder patterns, thermal gravimetric analysis, and model construction and topological analysis of MPF-3.

Chapter 4 relates the thermal response of a 3D flexible framework with $CdSO_4$ topology. The data in Chapter 4 has yet to be published. The initial synthesis and the synthesis of a single-crystal quality sample were developed by Evan Hurley. The single-crystal temperature dependent X-ray diffraction data were collected by Chunhua Hu. Synchrotron powder diffraction data were collected by Matthew Suchomel of Argonne National Labs. The author performed all structural analyses, both experimental and theoretical, using X-ray powder patterns and topological models

This thesis contains three distinct chapters to discuss interrelated porphyrin frameworks. Especially, we examine the idea that the structure of a framework can be correlated to its function. In Chapter 2, a topological analysis of the pyridyl porphyrin frameworks was conducted to look for trends in structural control. It was revealed that the coordination environment around the metal, the porphyrin type, and the metal to porphyrin stoichiometric ratio all played key roles in the determining the final topology. This chapter did not seek to examine functions or properties of the frameworks analyzed. Instead, the reasoning behind the need to precisely control framework assembly was presented. The ability to dictate the structure of a material allows structural types with desired properties to be engineered into the final product.

Chapter 3 and Chapter 4 both show the structural effects on the function of porphyrin frameworks. The unusual topology and interdigitation of MPF-3 and the noninterpenetrated $CdSO_4$ topology of E-MOF-1 are examined in Chapter 3 and 4, respectively, and the relationship between structure and flexibility is discussed.

1.5 References

1. Batten, S. R.; Neville, S. M.; Turner, D. R. *Coordination Polymers Design, Analysis and Application*; The Royal Society of Chemistry: Cambridge, 2009.
2. For reviews on flexible frameworks, see: (a) Fletcher, A. J.; Thomas, K. M.; Rosseinsky, M. J. *J. Solid State Chem.* **2005**, *178*, 2491. (b) Kitagawa, S.; Uemura, K. *Chem. Soc. Rev.* **2005**, *34*, 109. (c) Uemura, K.; Matsuda, R.; Kitagawa, S. *J. Solid State Chem.* **2005**, *178*, 2420.
3. DeVries, L. D.; Choe, W. *J. Chem. Crystallogr.* **2009**, *39*, 229.
4. For discussions on the terminology of coordination polymers and metal organic frameworks: (a) Biradha, K.; Ramanan, A.; Vittal, J. J. *Cryst. Growth Des.* **2009**, *9*, 2969. (b) O'Keeffe, M. *Chem. Soc. Rev.* **2009**, *38*, 1215. (c) Tranchemontagne, D. J.; Mendoza-Cortés, J. L.; O'Keeffe, M.; Yaghi, O. M. *Chem. Soc. Rev.* **2009**, *38*, 1257. (d) Kitagawa, S.; Kitaura, R.; Noro, S. *Angew. Chem. Int. Ed.* **2004**, *43*, 2334.
5. (a) Shimomura, S.; Horike, S.; Matsuda, R.; Kitagawa, S. *J. Am. Chem. Soc.* **2007**, *129*, 10990. (b) Cussen, E. J.; Claridge, J. B.; Rosseinsky, M. J.; Kepert, C. J. *J. Am. Chem. Soc.* **2002**, *124*, 9574. (c) Kubota, Y.; Takata, M.; Matsuda, R.; Kitaura, R.; Kitagawa, S.; Kobayashi, T. C. *Angew. Chem. Int. Ed.* **2006**, *45*, 4932. (d) Ma, S. Q.; Sun, D. F.; Wang, X. S.; Zhou, H. C. *Angew. Chem. Int. Ed.* **2007**, *46*, 2458. (e) Fletcher, A. J.; Cussen, E. J.; Bradshaw, D.; Rosseinsky, M. J.; Thomas, K. M. *J. Am. Chem. Soc.* **2004**, *126*, 9750. (f) Kondo, A.; Noguchi, H.; Carlucci, L.; Proserpio, D. M.; Ciani, G.; Kajiro, H.; Ohba, T.; Kanoh, H.; Kaneko, K. *J. Am. Chem. Soc.* **2007**, *129*, 12362. (g) Kitaura, R.; Seki, K.;

Akiyama, G.; Kitagawa, S. *Angew. Chem. Int. Ed.* **2003**, *42*, 428. (h) Horike, S.; Tanaka, D.; Nakagawa, K.; Kitagawa, S. *Chem. Commun.* **2007**, 3395. (i) Llewellyn, P. L.; Bourrelly, S.; Serre, C.; Filinchuk, Y.; Férey, G. *Angew. Chem. Int. Ed.* **2006**, *45*, 7751. (j) Chen, B. L.; Ma, S. Q.; Zapata, F.; Fronczek, F. R.; Lobkovsky, E. B.; Zhou, H. C. *Inorg. Chem.* **2007**, *46*, 1233. (k) Maji, T. K.; Matsuda, R.; Kitagawa, S. *Nat. Mater.* **2007**, *6*, 142. (l) Ohba, M.; Kaneko, W.; Kitagawa, S.; Maeda, T.; Mito, M. *J. Am. Chem. Soc.* **2008**, *130*, 4475. (m) Dybtsev, D. N.; Chun, H.; Kim, K. *Angew. Chem. Int. Ed.* **2004**, *43*, 5033.

6. Serre, C.; Mellot-Draznieks, C.; Surble, S.; Audebrand, N.; Filinchuk, Y.; Férey, G. *Science* **2007**, *315*, 1828.
7. Tanaka, D.; Nakagawa, K.; Higuchi, M.; Horike, S.; Kubota, Y.; Kobayashi, L. C.; Takata, M.; Kitagawa, S. *Angew. Chem. Int. Ed.* **2008**, *47*, 3914.
8. Choi, E.-Y.; DeVries, L. D.; Novotny, R. W.; Hu, C.; Choe, W. *Cryst. Growth Des.* **2010**, *10*, 171.

CHAPTER 2

CLASSIFICATION OF COORDINATION POLYMERS FORMED FROM PYRIDYL PORPHYRIN BUILDING UNITS

2.1 Introduction

Topological control of self-assembled coordination polymers is an important theme in materials chemistry, but remains a significant challenge for chemists seeking to synthesize new materials with tailored properties.[1-3] Although a priori predictions of solid state organization remain difficult, it is possible to generate a wide variety of self-assembled coordination polymers by the careful selection of organic and inorganic components.[3,4] For example, the ditopic ligand 4,4'-bipyridine shows various structural motifs when combined with transition metals, including 1D ladder, 1D chain, 1D railroad, 2D square grid, 2D hexagonal grid, 2D double-layer, and 3D undulated grid.[5-8] Switching to a tritopic ligand such as 1,3,5-tris[4-pyridyl(ethenyl)]benzene or 2,4,6-tris(4-pyridyl)1,3,5-trazine has produced various 3D nets.[4]

Compared with ditopic and tritopic ligands, tetratopic ligands are relatively rarely used as molecular building blocks. Among the available tetratopic ligands[9-11], we and others are particularly interested in the tetraarylporphyrins and their use in coordination polymers.[11-18] Porphyrins are important materials because of their exceptional photochemical and catalytic properties, which enable their use in sensors, catalysts, and

other applications.[12] These macrocycles often possess approximate D_{4h} symmetry, a point group rarely encountered in organic chemistry. Therefore, such porphyrins are exotic ligands for building frameworks with unprecedented topology that might prove inaccessible using other types of ligands with different connectivity and symmetry.[11-18]

During the past decade, numerous porphyrinic coordination polymers have been reported[11-18]; however, the field of porphyrinic coordination polymers is still in its infancy compared with the rich porphyrin chemistry developed in recent decades. In this review, we focus on coordination polymers constructed from the pyridyl-based porphyrins, specifically 5,10,15,20-tetrapyridylporphyrin (H_2TPyP) and its less symmetrical derivatives 5-pyridyl-10,15,20-triphenylporphyrin (H_2MPyP), 5,10-dipyridyl-15, 20-diphenylporphyrin (cis-H_2DPyP), and 5,15-dipyridyl-10,20-diphenylporphyrin (trans-H_2DPyP), and their respective metalloporphyrins (Fig. 1).

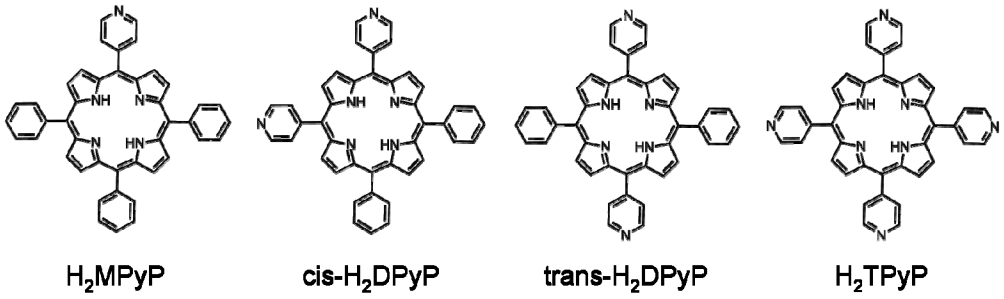

Figure 2.1. Four pyridyl-based porphyrin derivatives used as building units in the coordination polymers discussed in this review

Based on 44 analyzed porphyrin structures, we construct 17 classifications according to dimensionality, connectivity, and topology. We also discuss the structural trends found in porphyrinic coordination polymers and their interrelationships. Table 1 summarizes the compounds analyzed in this review, in which the structural reference

number used for each structure is listed next to the stoichiometric formula. For previous reviews of porphyrin coordination solids[13-17] and porphyrin supermolecules[19-21], see the works of Suslick[13,14], Goldberg[15,16], Proserpio[17], Kobuke[19], Alessio[20], and Hupp.[21]

2.2 Classification System

To understand the varied topologies possible for porphyrinic coordination polymers, a unified classification system was created. The 44 porphyrinic coordination polymers chosen to be analyzed were first separated by dimensionality: one-dimensional (1D), two-dimensional (2D), and three-dimensional (3D). These 44 coordination polymers where then assigned to one of 17 classifications based on metal-to-porphyrin geometry; porphyrin type; and porphyrin-to-metal ratio (see Table 2.1). The coordination geometry around the metal and the coordination number is listed in the *Metal node* column of Table 2.2. The number of axial connections to the metal center of a metallated porphyrin is detailed in the *Porphyrin node* column. The geometry and coordination number described in the *Metal node* column or the number of axial connections listed in the *Porphyrin node* column excludes any coordination to counter-ions or solvent. For example, the metal nodes of the "2D sheet-I" **12a** are listed with a square planar geometry and a coordination number of 4. However, the Pb atoms of the metal nodes sit in an octahedral environment with a coordination number of 6 because each node coordinates to two I atoms. The I atoms are not topologically significant for the purposes of classification. The metal-to-porphyrin ratio in Table 2.2 represents the ratio between porphyrin building units and the metals that connect neighboring porphyrins. Metal centers of porphyrins that do not coordinate to other porphyrins are not considered. This

ratio is important because altering the metal-to-porphyrin ratio of a porphyrinic coordination polymer can result in the formation of a different type of structure (such as a “2D sheet-I” instead of a “1D tape”).

Table 2.1 Pyridyl-based porphyrin coordination networks.

Refcode	Composition	Structural motif	Ref.
BAKJOM	$[(HgI_2)_2(H_2TPyP)]\cdot 2(TCE)$, 1	1D tape	22
BAKNOQ	$[(HgI_2)_2(Zn_{0.5}\ TPyP)]\cdot 4(TCE)$, 2	1D tape	22
BAKKED	$[(HgI_2)_2(Zn_{0.3}\ TPyP)]\cdot 4(TCE)$	1D tape	22
QODHEW	$[(HgI_2)_2(H_2TPyP)]\cdot 2(TCE)$	1D tape	23
QODHEW1	$[(HgI_2)_2(H_2TPyP)]\cdot 2(TCE)$	1D tape	23
UFOMEH	$[(HgI_2)_2(H_2TPyP)]\cdot C_{70}(TCE)\cdot(MeOH)$, 3	1D tape	24
HAZSOQ	$[(HgBr2)2(H_2TPyP)]\cdot 2(CHCl_3)$	1D tape	25
TUSHAQ	$[Ag(H_2TPyP)](NO_3)$, 4	1D rod	26
QARNOM	$[Ag(H_2TPyP)](PF_6)\cdot 1.5(TCE)\cdot(MeOH)\cdot(H_2O)$	1D rod	27
GETLAS	[(ZnMPyP)], 5	1D single zig-zag chain	28
NAZZUK	$[(cis\text{-}ZnDPyP)]\cdot(CH_3OH)$, 6	1D single zig-zag chain	29
YOVTEI	$[(ZnTPyP)]\cdot(C_6H_7N)$	1D single zig-zag chain	30
YOVTAE	[(ZnTPyP)], 7	1D single zig-zag chain	30
SAWJIK	$[(ZnTPyP)]\cdot 1.33(CHCl_3)$, 8	1D double zig-zag chain	31
BIJSAP	$[(trans\text{-}CoDPyP)_3]\cdot 4(C_3H_7NO)$, 9	1D double zig-zag chain	32
BABCEN	$[Zn_2(TPyP)_2]\cdot 5(C_6H_5NO_2)$, 10	1D ladder	33
IGOHOB	[FeTPyP], 11	2D grid	34
IGOHOB01	[FeTPyP]	2D grid	34
BAKPOS	$[(HgBr_2)_2(H_2TPyP)]\cdot 6(TCE)$	2D sheet-I	22
BAKREK	$[(HgI_2)_2(ZnTPyP)]\cdot 4(TCE)$	2D sheet-I	22
BAKKIH	$[(PbI_2)(H_2TPyP)]\cdot 4(TCE)$, 12a	2D sheet-I	22
BAKNEG	$[(CdI_2)(H_2TPyP)]\cdot 4(TCE)$	2D sheet-I	22
UFOMAD	$[Pb(NO_3)_2\cdot\ (H_2TPyP)]\cdot C_{60}\cdot 6(TCE)$, 7b	2D sheet-I	24
FEWGEU	$[Ag_2(H_2TPyP)]\cdot(m\text{-}C_6H_4NH_2Cl)_4\cdot 2(C_7H_7O_3S)$, 13	2D sheet-II	35
FEWGOE	$[Ag_2(ZnTPyP)]\cdot(CH_3C_6H_5\ SO_3)_2\cdot(DMA)]$, 14	2D sheet-II	35
TUSGIX	$[Ag_4(H_2TPyP)_3]\cdot 4(NO_3)$, 15	2D sheet-III	26
FEWGAQ	$[Ag_2(H_2TPyP)]\cdot 2(CF_3SO_3)$, 16	2D undulated tape	35
FEWGIY	$[Ag_2(ZnTPyP)_2]\cdot(m\text{-}C_6H_4NH_2)\cdot 2(CF_3SO_3)$, 17	2D hybrid net	35
PIZJEN	$[Cu_2(TPyP)]\cdot(BF_4)$, 18	3D net-I (pts)	18
YOVTOS	$[(ZnTPyP)]\cdot 3(H_2O)$, 19	3D net-II (nbo)	30
YOVTIM	$[(ZnTPyP)]\cdot(MeOH)\cdot 2(H_2O)$	3D net-II (nbo)	30
SAZQEQ	$[(ZnTPyP)]\cdot 1.33(CHCl_3)$	3D net-II (nbo)	31
CAYSOK	$[(MnTPyP)]\cdot 10(H_2O)$	3D net-II (nbo)	37
CAYSIE	$[(CoTPyP)]\cdot 2(CH_3COOH)\cdot 2(H_2O)$	3D net-II (nbo)	37
CAYYEG	$[(MnTPyP)]\cdot 2(EtOH)\cdot 4(H_2O)$	3D net-II (nbo)	37
QANSEE	$[(ZnTPyP)]\cdot 1.6(C_2H_4O_2)$	3D net-II (nbo)	38
CATDEH	$[(trans\text{-}ZnDPyP)]\cdot 0.33(MeOH)$	3D net-II (nbo)	39
CATDIL	$[(trans\text{-}ZnDPyP)]\cdot 0.33(C_6H_{12})$	3D net-II (nbo)	39
CAYRIE	$[(trans\text{-}ZnDPyP)]\cdot 0.33(C_2H_6O)$	3D net-II (nbo)	39
CAYROK	$[(trans\text{-}ZnDPyP)]$	3D net-II (nbo)	39
CAZGOZ	$[Fe(FeTPyP)_3]\cdot 2(Mo_6O_{19})\cdot 38(H_2O)$, 20	3D net-III (pcu)	40
TUSGUJ	$[Ag_8(ZnTPyP)_7]\cdot 8(NO_3)$, 21	3D net-IV	26
TUSGOD	$[Ag_2(H_2TPyP)]\cdot(NO_3)$, 22	3D net-V	26
SOBTUY	$[Cd_2(PdTPyP)]\cdot 2(NO_3)\cdot(py)\cdot 8.6(H_2O)$, 23	3D net-VI	11

TCE = tetrachloroethane; DMA = N,N'-dimethylacetamide; py = pyridine

pts- platinum sulfide net, **nbo**- niobium oxide net, **pcu**- primitive cubic

Table 2.2 Classification of coordination porphyrin networks

Classification	Node		Porphyrin[c]	M:Por[d]	# Nets[e]
	Metal[a]	Porphyrin[b]			
1D tape	bent (~90°)	—	TPyP, *M*TPyP	2:1	7
1D rod	linear (~180°)	—	TPyP	1:1	2
1D single zig-zag chain	—	1	MPyP, *cis*-DPyP, TPyP	1:1	4
1D double zig-zag chain	—	1 and 2	*trans*-DPyP, TPyP	1:1	2
1D ladder	—	1 and 2	TPyP	1:1	1
2D undulated tape	bent (~100°)	—	TPyP	2:1	1
2D grid	—	2	TPyP	1:1	2
2D sheet-I	square planar	—	TPyP, *M*-TPyP	1:1	5
2D sheet-II	linear (~180°)	—	TPyP, *M*-TPyP	2:1	2
2D sheet-III	T-shape	—	TPyP	4:3	1
2D hybrid net	distorted tetrahedral, bent (~90°)	1	*M*TPyP	XXX	1
3D net-I (**pts**)	tetrahedral	—	TPyP	1:1	1
3D net-II (**nbo**)	—	2	*M*TPyP, *trans*-*M*DPyP	1:1	11
3D net-III (**pcu**)	octahedral	2	*M*TPyP	1:1	1
3D-net-IV	T-shape	1	*M*TPyP	XXX	1
3D net-V	linear (~180°)	—	TPyP	2:1	1
3D net-VI	bent (~90°)	—	TPyP	1:1	1

[a] Geometry that connects metal node to porphyrin; [b] Number of axial connections to another porphyrin or a metal node; [c] Type of porphyrin that formed specified network; [d] Ratio of structurally important metals to porphyrins in network; [e] Number of example coordination networks for each classification

2.3 1D Coordination Polymers

2.3.1 1D Tapes

The 1D tape motif resembles a length of "tape" extending infinitely in one dimension. This tape consists of porphyrins linked together by metal nodes. In the case of **1** (Figure 2.2a), the porphyrins are of the TPyP type and the metal nodes are mercury atoms with iodide ions attached at tetrahedral positions. The resulting 1D planar array can be partially metallated to produce **2** (Figure 2.2b). The general formula of this 1D tape

series is $[(HgX_2)_2M_yTPyP]\cdot n(TCE)$, where X = Br, I; M = Zn, or H_2; n = 2,4,6 (TCE= tetrachloroethane)].[22-23] These 1D tape structures can hold various amounts of TCE molecules in between the tapes[22-23], and even accommodate C_{70} molecules as can be seen in **3** (Figure 2.2c). Pan *et al.* also reported identical 1D tape motif using $CHCl_3$ as a solvent[25]. The 1D tape motif is interesting because it is observed in multiple 2D variants.[22,35]

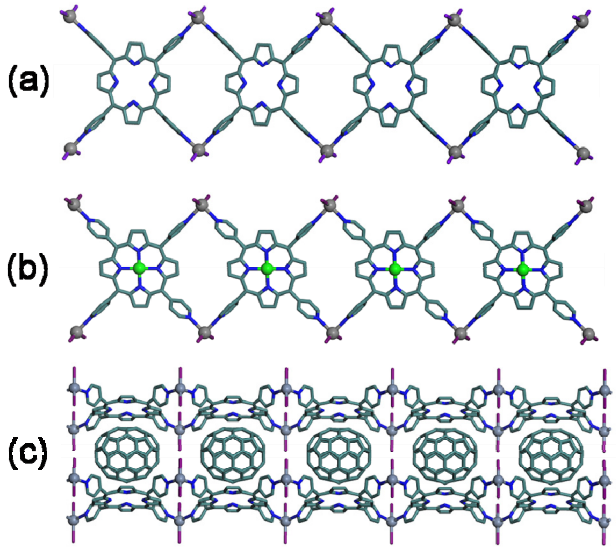

Figure 2.2. Variations of the 1D tape structural motif in (a) **1**, $(HgI_2)_2(H_2TPyP)]\cdot 2(TCE)$, (b) **2**,$[(HgI_2)_2(Zn_{0.5}\ TPyP)]\cdot 4(TCE)$, and (c) **3**, $[(HgI_2)_2(H_2TPyP)]\cdot C_{70}(TCE)\cdot(MeOH)$ are all approximately planar, and utilize fully coordinated TPyP units.

2.3.2 1D Rod

The 1D rod motif is so named because a single "rod" of metal nodes can be visualized as the backbone of the porphyrin network (Figure 2.3). In **4** only two pyridyl arms of each H_2TPyP molecule are coordinated to a silver metal node.[26] The uncoordinated nature of the "extra" pyridyl arms is puzzling until the synthesis conditions are examined. The silver to porphyrin ratio is 1:1, and as such, there are not enough silver

atoms to fully coordinate all of the pyridyl arms.[27] With a larger concentration of silver atoms, a 2D structure would be possible. This type of porphyrin rod formation is unusual, and has only been demonstrated by porphyrin networks containing silver salts such as $Ag(NO_3)$[26] and $AgPF_6$.[27]

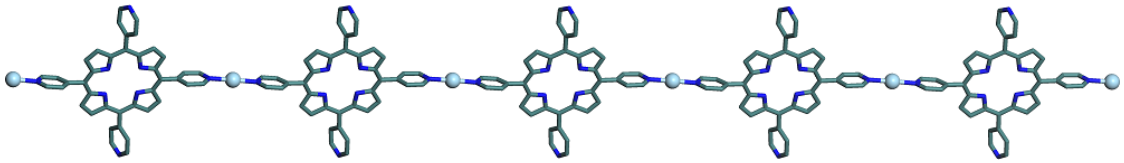

Figure 2.3. The 1D rod in **4**, $[Ag(H_2TPyP)](NO_3)$.

2.3.3 1D Single Zig-Zag Chains

A 1D single zig-zag chain is a common structural motif found in 1D porphyrin coordination solids (Figure 2.4). This motif requires a metallated porphyrin because the only connection point is the metal node in the center of the porphyrin. It is also noteworthy to mention that Zn atoms in these porphyrins are all five coordinated. Zinc-metallated MPyPs are linked through their zinc metal centers to one of pyridyl arms of a neighboring ZnMPyPs[28] as illustrated in **5**. The resulting geometry is the "zig-zag" pattern. Other pyridyl-based porphyrins such as cis-ZnDPyP (**6**) and ZnTPyP (**7**) also form similar zig-zag patterns[29], despite additional uncoordinated pyridyl arms. A plausible explanation for this is the competition for pyridyl coordination sites from solvent molecules hydrogen bonded to the vacant pyridyl arms.[30]

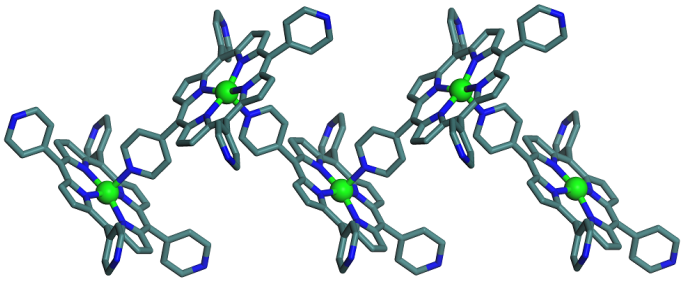

Figure 2.4. 1D single zig-zag chain in **7**, [(ZnTPyP)]

2.3.4 1D Double Zig-Zag Chains

The 1D double zig-zag chain **8** is closely related to the 1D zig-zag chains mentioned previously (Figure 2.5a,b).[31] A metallated porphyrin is again needed to provide a metal node; however, in this topology there are fewer uncoordinated pyridyl arms. Unlike the *single* chain, in this *double* chain motif, there are two distinct metalloporphyrin units found; five- and six-coordinate zinc(II) ions in a 2:1 ratio (Figure 2.5a). This ratio of metalloporphyrin coordination environments will be especially important. As shown in Figure 2.5b, Pan *et al* reported the identical 1D motif of **9**, but the two networks display a notable difference in stability.[31,32] The structure **8** is highly sensitive to solvent loss, and rapidly becomes amorphous upon solvent removal.[31] In contrast, the structure **9** retains crystallinity in the absence of solvent molecules.[32] This is a prime example of the same topology displaying significantly different physical properties.

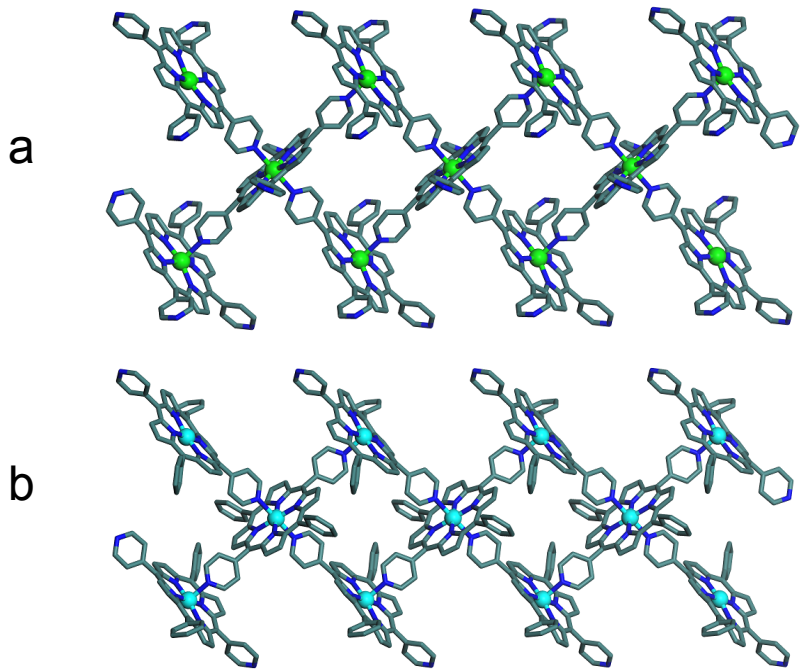

Figure 2.5. 1D double zig-zag chains in (a) **8**, [(ZnTPyP)]·1.33($CHCl_3$), and (b) **9**, [(trans-CoDPyP)$_3$]·4(C_3H_7NO)

2.3.5 1D Ladder

The 1D ladder network of **10** is illustrated in Figure 2.6.[33] The ladder configuration is related to both the 1D single zig-zag chain and the 1D double zig-zag chain. A major difference between this ladder and 1D double zig-zag chain is the ratio between five- and six-coordinate ZnTPyP. The ratio is 2:1 for 1D double zig-zag chain and 1:1 for 1D ladder. Therefore, this ratio is an important variable to control the topology of 1D porphyrin arrays. The formation of this 1D ladder instead of a 1D single zig-zag chain or a 1D double zig-zag chain may be influenced by the use of nitrobenzene as a solvent.[33] Diskin-Posner *et al* propose that the rigidity and polarity of nitrobenzene provide a significant influence in the formation of **10**.[33]

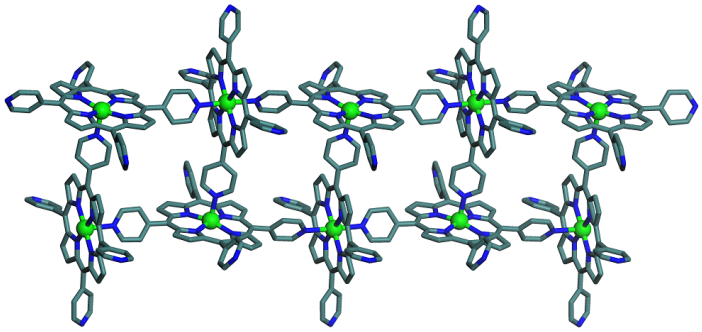

Figure 2.6. 1D ladder motif in **10**, $[Zn_2(TPyP)_2]\cdot 5(C_6H_5NO_2)$

2.4 2D Coordination Polymers

2.4.1 2D Grid

The 2D grid of **11** is shown in Figure 2.7.[34] An individual FeTPyP porphyrin is connected to four neighboring ones; two through its metal center and the other two through its pyridyl arms. This coordination mode leaves two pyridyl arms uncoordinated. The resulting 2D grid pattern shows two different stacking sequences; AB or ABCD. This 2D network is exceptionally robust and thermally stable up to 550 ºC under nitrogen.[34] In this motif, all the Fe(II) ions inside the porphyrin ring are octahedrally coordinated. As the ratio between the five- and six-coordination metal centers inside the porphyrin changes from 100%, 67%, 50%, to 0%, the respective structural motifs varies: 1D single zig-zag chain, 1D double zig-zag chain, 1D ladder, and finally to 2D grid. With one exception, the synthesis of **11** is significantly different from the synthesis methods used for the 1D single zig-zag chain, 1D double zig-zag chain, and 1D ladder.[28-34] The compound **11** was synthesized under solvothermal conditions, and the 1D double zig-zag chain compound **9** uses cobalt in DMF and a similar solvothermal process as **11**.[32,34] The similarities between compound **11** and compound **9** do not end at the synthesis techniques because cobalt and iron both prefer octahedral coordination.

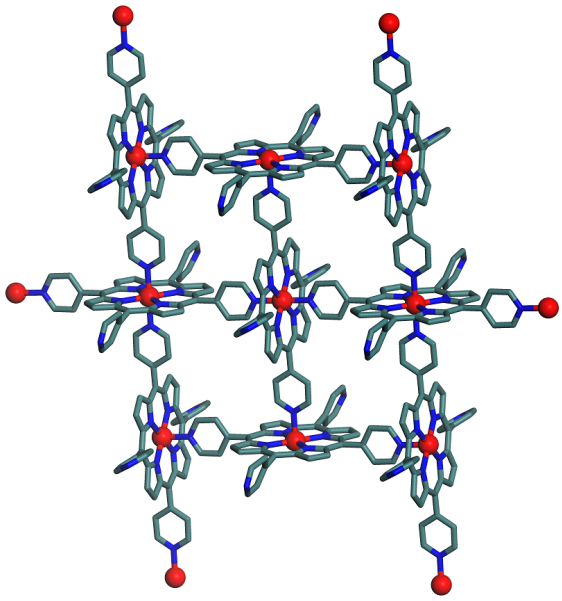

Figure 2.7. 2D grid-I motif in **11**, FeTPyP

2.4.2 2D Sheets

The 2D sheet-I is a variation of the 1D tape motif described earlier (Figure 2.8a,b). The tape motif extends in two perpendicular directions, while the metal node changes from tetragonal HgI_2 to octahedral PbI_2 or CdI_2.[22] The connectivity of the metal node to the porphyrin sheet is square planar as seen in **12a** and **12b**.[22,24] Structure **12a** consists of H_2TPyP units linked by PbI_2 as shown in Figure 2.8a, that connect four neighboring H_2TPyP units.[22] This 2D sheet-I pattern (**12b**) can accommodate C_{60} molecules in the space between the 2D sheets, as illustrated by Figure 2.8b.[24] 2D sheet-II pattern of **13** (Figure 2.9a) is a variation of the previously discussed 1D rod with a greater stoichiometric ratio of silver atoms to porphyrin units: 2:1 versus 1:1 for the 1D rod.[26,35] A metallated version of this 2D sheet-II **14** is shown in Figure 2.9b has also reported.[35] Recently Ohmura *et al.* reported a similar 2D sheet pattern using CuTPyP units and Cu

paddle-wheel clusters.[36] The 2D sheet-III shown by **15** (Figure 2.10) also uses silver nodes to connect the porphyrin units in a T-shaped geometry.[26] The metal-to-porphyrin ratio is again a major variable in forming a network that is topologically different from **4**, **13**, or **14**. As stated above, the 2D sheet-II (**13**) has a silver atom to porphyrin ratio of 2:1, but the silver atom to porphyrin ratio of **15** is 4:3.[26,35] Other than this ratio, the synthetic conditions are essentially identical.[26,35] The effective coordination number of the metal connector plays an important role in the 2D sheets shown here. The 2D sheet pattern varies as the effective coordination number changes from 4 (2D sheet-I) to 3 (2D sheet-III), and to 2 (2D sheet-II).

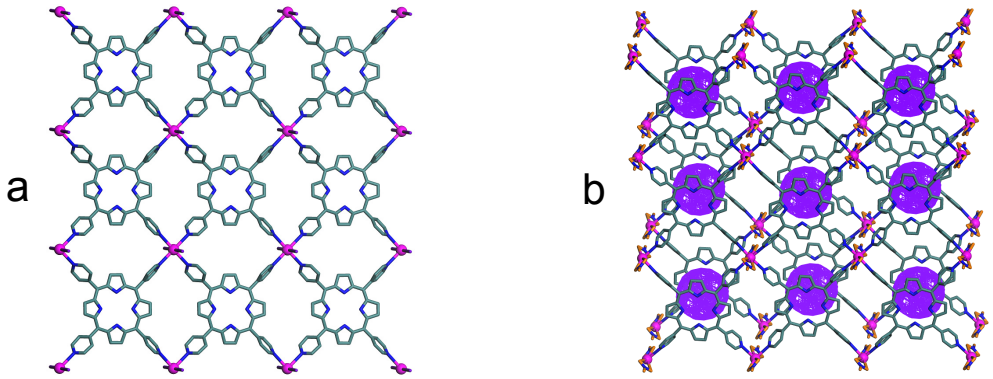

Figure 2.8. (a) 2D sheet-I in **12a**, $[(PbI_2)(H_2TPyP)]\cdot 4(TCE)$, (b) 2D sheet-I with C_{60} molecules found in **12b**, $[(Pb(N_2O_6)(H_2TPyP)]\cdot C_{60}\cdot 6(TCE)$

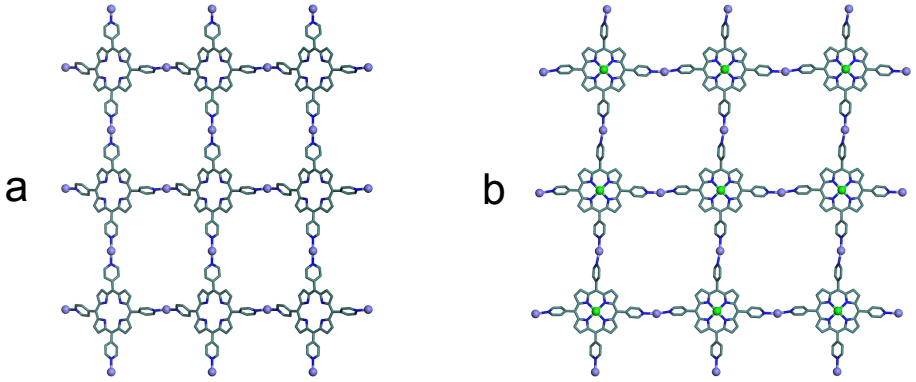

Figure 2.9. (a) 2D sheet-II in **13**, $[Ag_2(H_2TPyP)]\cdot(m\text{-}C_6H_4NH_2Cl)_4\cdot 2(C_7H_7\ SO_3)$, (b) 2D sheet-II with ZnTPyP, **14**, $[Ag_2(ZnTPyP)]\cdot(CH_3C_6H_5SO_3)_2\cdot(DMA)$

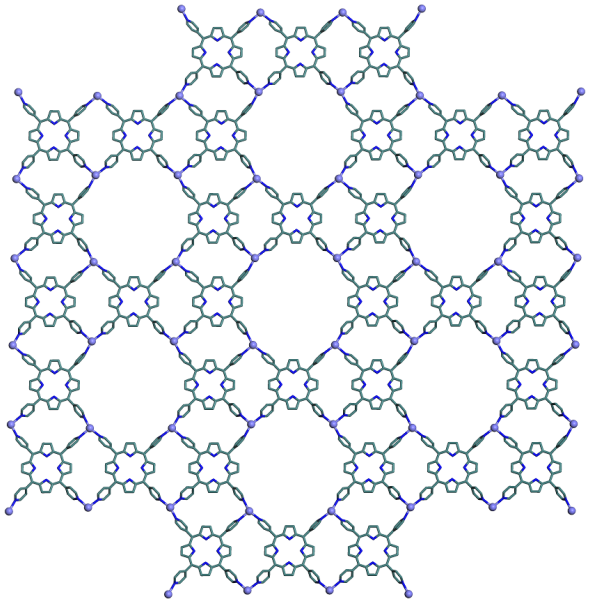

Figure 2.10. 2D sheet-III in **15**, $[Ag_4(H_2TPyP)_3]\cdot 4(NO_3)$.

2.4.3 2D Undulated Tape

The 2D undulated tape **16** in Figure 2.11 possesses the same connectivity as **13**, but has a significantly different topology.[35] It also has the same silver atom to porphyrin ratio as **13** (2:1).[35] The solvents used in each synthesis may be a contributing factor to the differing structures. It was found that for **16**, two *m*-chloroaniline molecules were tetrahedrally coordinated to each silver atom along with two pyridyl arms.[35] These solvent molecules may block the pyridyl arms from the coordination environment that would form **13** and so compound **16** forms instead. Structure **16** can also be viewed as a 2D variation of the 1D tape motif.[35] Similarly, the metal node connection geometry of **16** is similar to 1D tape (**1**); however, instead of a planar array, the metal nodes connect to porphyrins above and below the plane of the 1D tape.

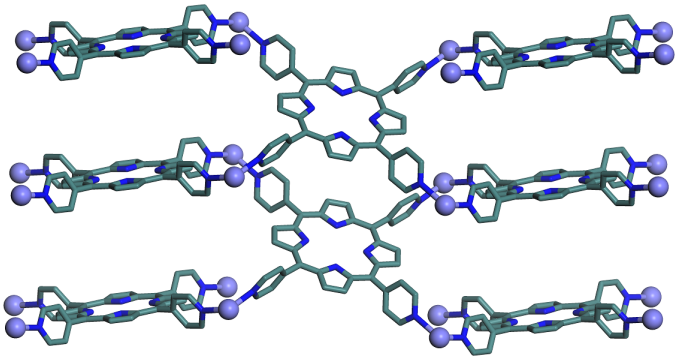

Figure 2.11. 2D undulated tape motif in **16**, $[Ag_2(H_2TPyP)]\cdot 2(CF_3SO_3)$.

2.4.4 2D Hybrid Net

The 2D hybrid net of **17** shows the combination of a 1D tape layer and a 1D single zig-zag chain layer (Figure 2.12a,b).[35] As seen in Figure 2.12a, **17** can be visualized as a 1D single zig-zag chain layer sandwiched between two 1D tape layers. The structure propagates in a "stair-step" pattern with the 1D tape motif as the base, and the 1D zig-zag layers as the upright (Figure 2.13a,b). Another remarkable feature of this network is that it contains three different coordination environments and two different metal nodes.[35] The two metal nodes are the zinc atoms in the center of the porphyrins and the silver atoms that make up the connectivity of the 1D tape layers. All of the porphyrins (i.e., those in the 1D single zig-zag chain layer and those in the 1D tape layer) are metallated with zinc. These zinc atoms in the porphyrin are all five-coordinate and are axially connected to the pyridyl arm of a neighboring porphyrin. The silver nodes display two different coordination geometries, depending on their position in the network. The silver nodes at the junction of each "stair-step" section are four-connected (Figure 2.13a) while the silver nodes at the non-shared edges of the "stairs" are two-connected (Figure 2.13b). Finally, **17** is notable because it is a bimetallic framework using porphyrin units.

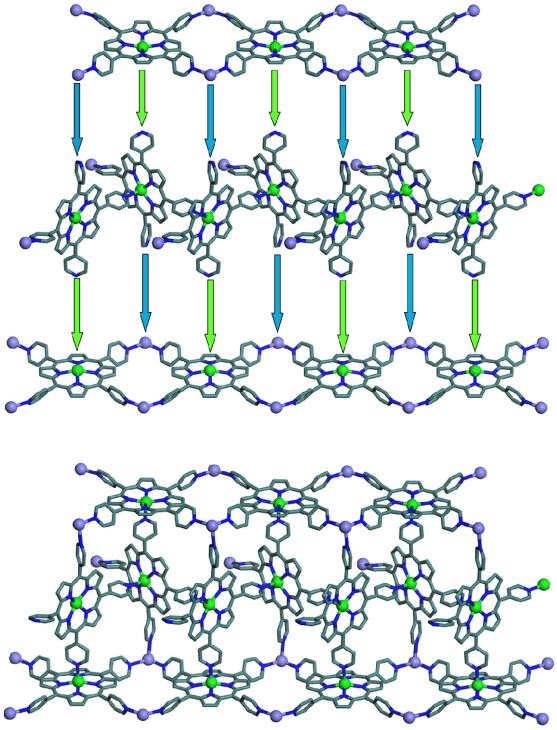

Figure 2.12. a Visualization of 1D tape and 1D single zig-zag motifs present in 17. **b** Assembled ‘‘stair-step’’ 2D hybrid net in 17, [Ag2(ZnTPyP)2]·(m-C6H4NH2) ·2(CF3SO3)

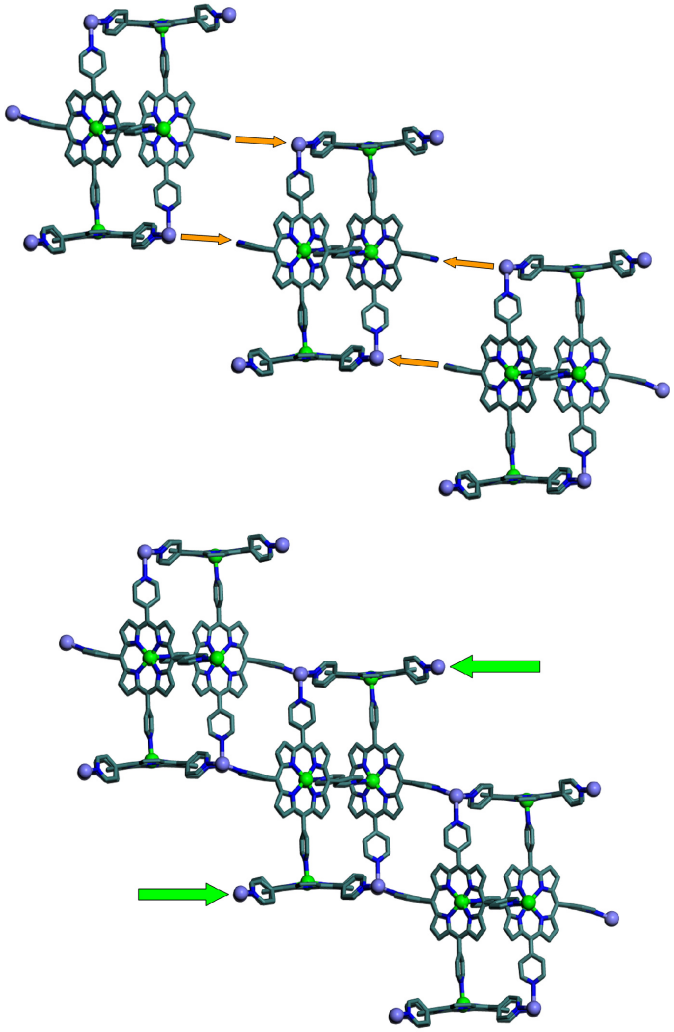

Figure 2.13. a Alternate view of the propagation of 17, emphasizing the four-coordinate silver connections (orange arrows) and showing the ‘‘stair’’ units of Fig. 12 in a different view. **b** Assembled view showing the four-coordinate silver atoms connected and the two coordinate silver connections (green arrows)

2.5 3D Coordination Polymers

2.5.1 3D Net-I

Figure 2.14 shows the **pts** (or PtS structure type) net **18**, synthesized by Robson and coworkers.[18] In this structure, pyridyl groups of CuTPyP molecules coordinate to Cu(I) ions, forming a tetrahedral geometry. There are an equal number of tetrahedral

copper atoms and square planar CuTPyP. These two metal nodes connect in an alternating pattern and form the open channel structure of a **pts** net[4], demonstrating that *ca.* 70% of the cell volume is void.[17] However, this framework is not robust and the channels collapse upon the loss of solvent molecules.[18]

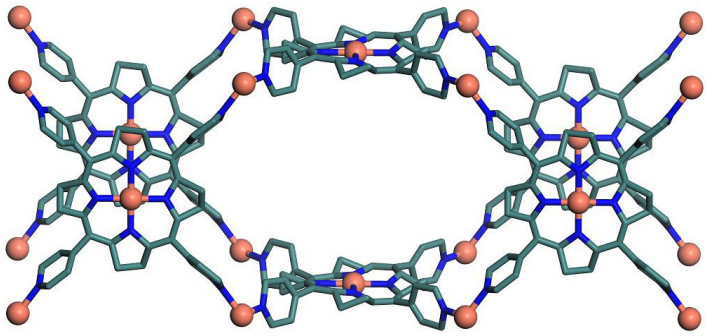

Figure 2.14. 3D net-I (pts) in 18, [Cu(CuTPyP)]·(BF4)

2.5.2 3D Net-II

The 3D **nbo** (NbO structure type) net of **19** was first reported by Goldberg[30], and the same pattern has been studied extensively.[30,37-39] As shown in Figure 2.15, this net is significantly distorted from its ideal **nbo** topology[4], creating large, open hexagonal channels. This structure can accommodate various solvent molecules (e.g. water, methanol, acetic acid, and cyclohexane) inside the hexagonal channel.[30,37-39] Using trans-DPyP molecular building blocks, Hosseini and coworkers reported a single-crystal-to-single-crystal transformation upon solvent exchange[38], thereby demonstrating the robustness of this framework.

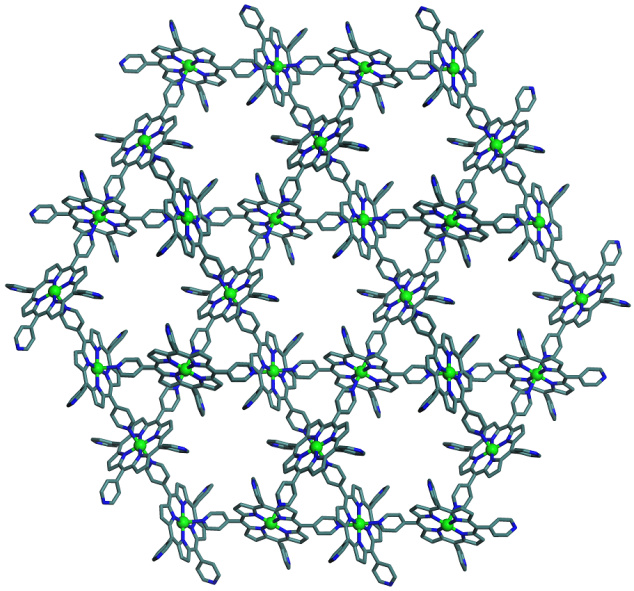

Figure 2.15. 3D net-II (nbo) in 19, [(ZnTPyP)]·3(H2O)

2.5.3 3D Net-III

The 3D net-III structure **20** contains two different six-coordinate Fe centers: the Fe center in the FeTPyP unit and the Fe node joining six surrounding porphyrins.[40] This forms a primitive cubic (**pcu**) network (Figure 2.16a) that shares the same octahedral connectivity of the 2D grid (**11**) shown earlier in Figure 2.7. However, the 2D "layers" of the 3D net-III consist of FeTPyP units and iron nodes, whereas **11** only contains FeTPyP units.[34,40] The connectivity of structure **20** can be viewed as a single 2D pattern being translated by (½ ½ ½) to form the observed AB packing (Figure 2.16b). In this example, the 2D layers are essentially identical; only the orientation of the layers changes (Figure 2.16c). The synthesis of **11** and **20** both use the solvothermal method and metallate the porphyrin in situ[34,40]; however, this is where the similarities end. The 2D structure (**11**) uses DMF as a solvent, whereas the 3D structure (**20**) uses water.[34,40] The metal sources also differ: ferrocene for **11** and $Fe_2Cl{\cdot}(H_2O)_4$ for **20**.[34,40] Perhaps the most significant

difference is the addition of MoO_3 to the synthesis of **20**.[40] The addition of this oxide is noteworthy because hexamolybdate $[Mo_6O_{19}]^{2-}$ clusters are formed during synthesis and the structure is cationic $[Fe_8(TPyP)_6]^{8+}$.[40] The clusters are centered in some of the large voids of the 3D FeTPyP network and the remaining adjacent voids contain water molecules.[40] These water-filled voids are arranged in an octahedral orientation around each hexamolybdate-filled void.[40] The presence of the hexamolybdate ion prevents any potential interpenetration, which is common in frameworks with such large voids.[4]

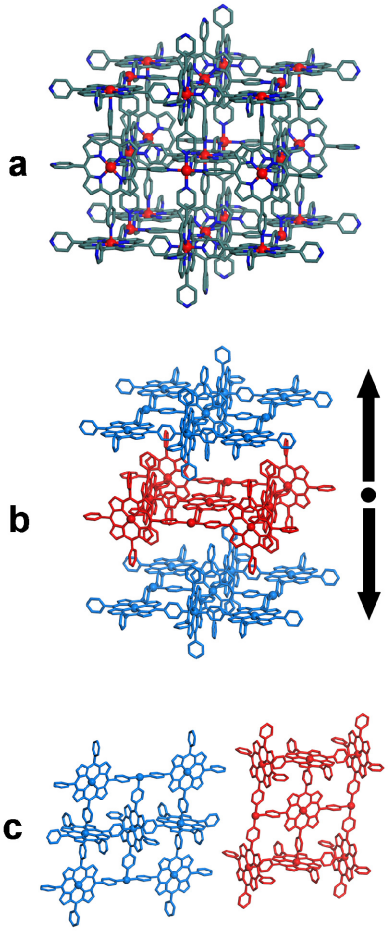

Figure 2.16. a 3D net-III (pcu) in 20, [Fe(FeTPyP)3]·2(Mo6O19)·38(H2O). **b** View of the 2D layers related by a (½½½) translation to form the AB packing of 20. The structure has been separated into individual layers to emphasize the (½½½) translation. **c** ‘‘A’’ and ‘‘B’’ layers in 20

2.5.4 3D Net-IV

The 3D net-IV **21** is shown in Figure 2.17.[26] The vertical (red in the figure) and horizontal (blue in the figure) layers connect through the axial coordination of the ZnTPyP molecules of each layer to a “rod” (green in the figure) of porphyrins running down the center of the channel. The vertical and horizontal layers are analogous to a zinc

metallated version of the 2D sheet-III (**15**) mentioned previously (Figure 2.18), and the "rod" is made of stacked ZnTPyP molecules. In addition, the vertical and horizontal 2D layers are interpenetrated through the large void space of the other 2D layers (Figure 2.19).[26] The red section in Figure 2.18 corresponds to both the vertical red layers in Figure 2.17 and the vertical red layers in Figure 2.19. This interpenetration is not limited to one set of vertical and horizontal layers. There is a second set of parallel 2D layers running along each vertical and horizontal sheet that also interpenetrates the other 2D layers (Figure 2.19). This second set of 2D layers is connected to the neighboring porphyrin "rods," and each 2D layer is connected to three other layers as shown in Figure 2.20.[26] It should also be noted that not all of the ZnTPyP porphyrins are structurally coordinated. The stacked ZnTPyP porphyrins that make up each "rod" are not coordinated, and neither are the porphyrins located where the 2D sheets intersect (see the central area of Figure 2.20).

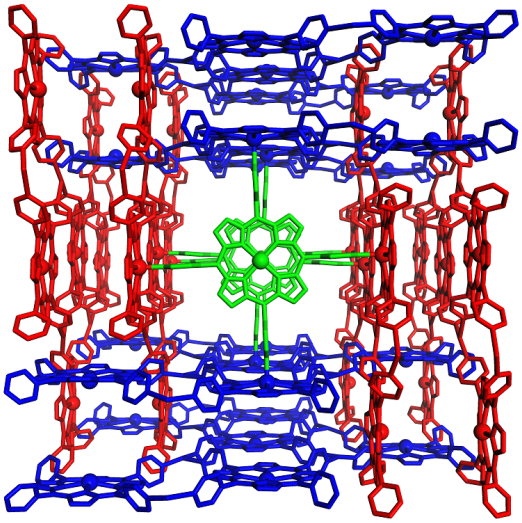

Figure 2.17. 3D net-IV in 21, [Ag8(ZnTPyP)7]·8(NO3)

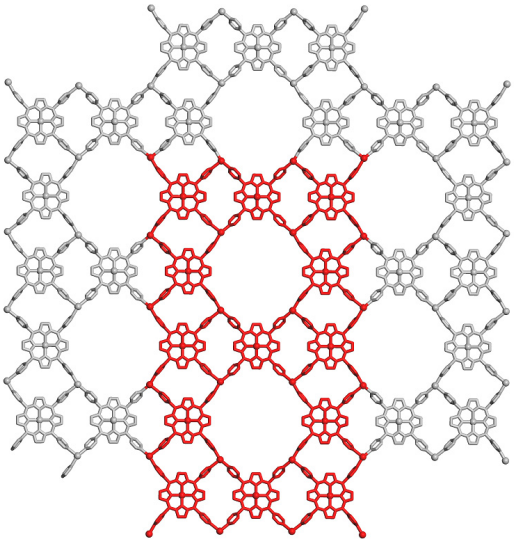

Figure 2.18. 2D layer of 21, a variation of 2D Sheet-III 15. The highlighted red section is a ‘‘front’’ view of all of the red layers present in Figs. 17, 19, and 20

The synthesis conditions of **15** and **21** are remarkably the same except for two notable differences. Both structures were synthesized using the solvent layering method.[26] They share the same solvent metal layer (AgNO3 dissolved in dimethylamine), and the porphyrins used for each structure where dissolved in 3:1 TCE:MeOH.[26] The differences that separate **15** and **21** are the temperature of the synthesis (room temperature for **15** versus -20° C for **21**) and the use of freebase TPyP or ZnTPyP, respectively.[26] The framework pattern of **21** would be impossible without metallated porphyrins to connect the 2D layers.

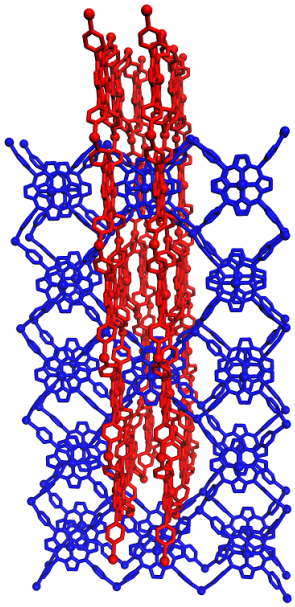

Figure 2.19. Interpenetration of the 2D layers of 21 through the large voids in each layer

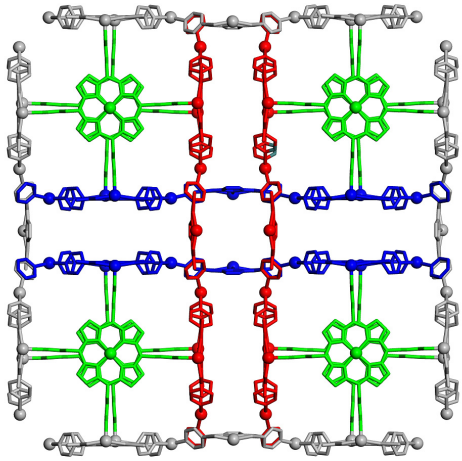

Figure 2.20. Alternate view of 21, showing the intersection of the 2D layers at the voids where they interpenetrate, and the pattern in which the porphyrin ‘‘rods’’ (green) connect to the 2D layers (red and blue)

2.5.5 3D Net-V

The 3D structure **22** is a 3D variation of the 2D sheet-II.[26] The main difference is that the silver atoms at the junctions are three coordinate instead of the two coordinate

silver atoms in the 2D sheets. The layers are joined by the NO_3^- ions to form the 3D structure of **22** (Figure 2.21).

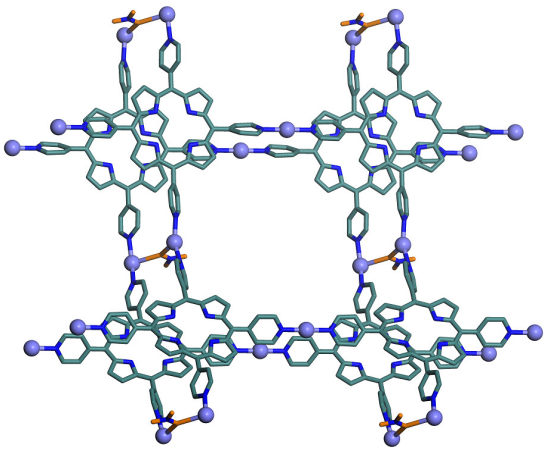

Figure 2.21. 3D net-V in 22, [Ag2(H2TPyP)]·(NO3)

Robson and coworkers synthesized **23**.[11] In this structure, Cd atoms are used as two different types of connectors: linear connectors (N-Cd-N, 180˚) and bent L-shaped connectors (N-Cd-N, 103˚). The porphyrin linkers (PdTPyPs) are joined by these Cd atoms to form 3D frameworks in which porphyrin molecules are all stacked along the [001] direction (Figure 2.22).

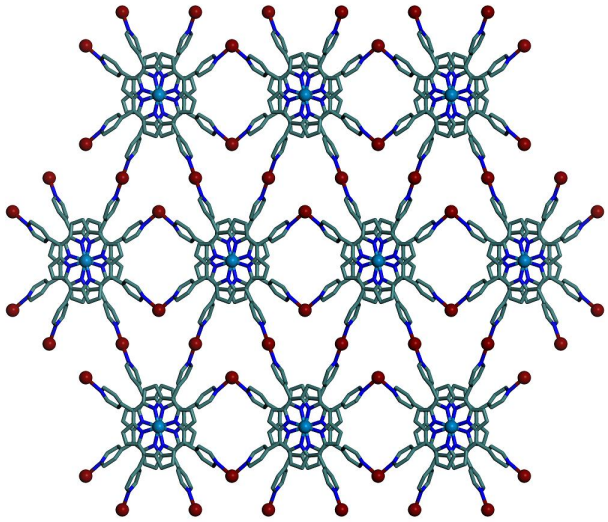

Figure 2.22. 3D net-VI in 23, [Cd2(PdTPyP)]·2(NO3)·(py)·8.6(H2O)

2.6 Synthetic Methods

This study has considered a total of 44 porphyrinic coordination polymers with various topologies, yet the synthetic methods employed in making these structures are not as varied as might be expected. Upon examination, three main synthetic methods are used to synthesize the structures detailed in this thesis: solvent layering, evaporation, and the solvothermal method.

The solvent layering method involves the addition of starting materials to two or more solvents. The solvents are layered on top of each other to either reduce the solubility of the product in a single layer to promote crystallization, or to slow diffusion between starting materials. The choice of the two (or more) solvents is important (based on polarity, viscosity, solubility, etc.). The 2D sheet-I in Fig. 7b was made by layering the metal source, dissolved in one solvent, over C60 and H_2TPyP dissolved in another solvent.[24]

The evaporation method involves simply allowing the reaction mixture to sit undisturbed for an extended period (days to weeks) while the solvent evaporates. The 1D ladder in Fig. 5 was formed using the evaporation method.[33]

The solvothermal method uses a pressure vessel to contain the reaction mixture while it is heated, under autogeneous pressure, to a certain temperature (usually greater than 100 °C) for a set time. The thermal ramping, reaction temperature, and duration can all be altered. The 2D grid in Fig. 6 was the product of solvothermal reaction between ferrocene and H2TPyP at 150 °C for 5 days in a Teflon lined autoclave.[34]

2.7 Conclusion

Numerous structural motifs are self-assembled from pyridyl-based porphyrin building units. Due to the intrinsic properties of porphyrin, these multi-dimensional porphyrinic coordination polymers and/or subsequent solids have potential as useful materials for practical applications in catalytic chemistry, optoelectronics, gas storage, and molecular magnets.[12] Topological control is important in providing the properties required for each of these applications. It is therefore essential to understand the underlying building principle of these porphyrin coordination solids. The metal coordination, porphyrin type, and metal-to-porphyrins ratio can all be used to produce varied structural motifs. A solid working knowledge of the effects of changing any one (or more) parameter(s) is the key to producing a coordination polymer with the desired topology. Many structures discussed in this paper can be thought of as being made of two distinct units: metalloligands and metal nodes. Kitagawa demonstrated that the physical properties of materials using metalloligands can be altered by using a different organic linker.[40] If a

correlation could be found between the properties and structure of such metalloligand-based frameworks, a material with tailored properties could be produced by combining different structural motifs. A structural understanding can be further utilized to engineer new types of functional 3D porous porphyrin frameworks.

2.8 References

1. Eddaoudi, M.; Kim, J.; Rosi, N.; Vodak, D.; Wachter, J.; O'Keeffe, M.; Yaghi, O. M. *Science* **2002**, *295*, 469.
2. O'Keeffe, M.; Eddaoudi, M.; Li, H.; Reineke, T.; Yaghi, O. M. *J. Solid State Chem*. **2000**, *152*, 3.
3. Robson, R. *J Chem Soc Dalton Trans* **2000**, 3735.
4. Öhrström, L.; Larsson, K. *Molecule Based Materials, The Structural Network Approach*; Elsevier: Amsterdam, 2005.
5. Noro, S.-I.; Kitaura, R.; Kondo, M.; Kitagawa, S.; Ishii, T.; Matsuzaka, H.; Yamashita, M. *J. Am. Chem. Soc.* **2002**, *124*, 2568.
6. Yaghi, O. M.; Li, H.; Davis, C.; Richardson, D.; Groy, T. L. *Acc. Chem. Res.* **1998**, *31*, 474.
7. Halder, G.J.; Kepert, C. J. *J Am Chem Soc.* **2002**, *124*, 2568.
8. Fletcher, AJ.; Cussen, E. J.; Bradshaw, D.; Rosseinsky, M. J. *J. Am. Chem. Soc.* **2004**, *126*, 9750.
9. Zheng, N. F.; Bu, X. H.; Feng, P. Y. *J. Am. Chem. Soc. 2004*, *124*, 9688.
10. Choe, W.; Kiang. Y.-H.; Xu, Z.; Lee, S. *Chem. Mater.* **1999**, *11*, 1776.
11. Abrahams, B. F.; Hoskins, B. F.; Robson, R. *J. Am. Chem. Soc.* **1991**, *113*, 3606.

12. Chou, J.-H.; Nalwa, H. S.; Kosal, M. E.; Rakow, N. A.; Suslick, K. S. *The Porphyrin Handbook*, Vol. 6; Academic Press: Orlando, 2000; p 43.

13. Choi, E.-Y.; Barron, P. M.; Novotny, R. N.; Hu, C.; Kwon, Y.-U.; Choe, W. *Cryst. Eng. Comm.* **2008**, 824.

14. Suslick, K. S.; Bhyrappa, P.; Chou, J.-H.; Kosal, M. E.; Nakagaki, S.; Smithenry, D. W.; Wilson, S. R. *Acc. Chem. Res.* **2005**, *38*, 283.

15. Goldberg, I. *Chem. Eur. J.* **2000**, *6*, 3863.

16. Goldberg, I. *Cryst. Eng. Comm.* **2002**, *4*, 109.

17. Carlucci, L.; Ciani, G.; Proserpio, D. M.; Porta, F. *Cryst. Eng. Comm.* **2005**, *7*, 78.

18. Abrahams, B. F.; Hoskins, B. F.; Michail, D. M.; Robson, R. *Nature* **1994**, *369*, 727.

19. Kobuke, Y. *Struct. Bond.* **2006**, *121*, 49.

20. Iengo, E.; Zangrando, E.; Alessio, E. *Acc. Chem. Res.* **2006**, *39*, 841.

21. Lee, S. J.; Hupp ,J. T. *Coord. Chem. Rev.* **2006**, *250*, 1710.

22. Sharma, C. V. K.; Broker, G. A.; Huddleston, J. G.; Baldwin, J. W.; Metzger, R. M.; Rogers, R. D. *J. Am. Chem. Soc.* **1999**, *121*, 1137.

23. Sharma, C. V. K.; Broker, G. A.; Rogers, R. D. *J Solid State Chem* **2000**, *152*, 253.

24. Sun, D.; Tham, F.; Reed, C. A.; Boyd, P. D. W. *Proc. Nat. Acad. Sci. USA* **2002**, *99*, 5088.

25. Pan, L.; Noll, B. C.; Wang, X. *Chem. Commun.* **1999**, 157.

26. Carlucci, L.; Ciani, G.; Proserpio, D. M.; Porta, F. *Angew. Chem. Int. Ed.* **2003**, *42*, 317.

27. Kondo, M.; Kimura, Y.; Wada, K.; Mizutani, T.; Ito, Y.; Kitagawa, S. *Chem. Lett.* **2000**, 818.

28. Shachter, A. M.; Fleischer, E. B.; Haltiwanger, R. C. *Chem. Commun.* **1988**, 960.

29. Deiters ,E.; Bulach, V.; Kyritsakas, N.; Hosseini, M. W. *New J. Chem.* **2005**, *29*, 1508.

30. Krupitsky, H.; Stein, Z.; Goldberg, I.; Strouse, C. E. *J. Inclusion. Phenom. Mol. Recog. Chem.* **1994**, *18*, 177.

31. Ring, D. J.; Aragoni, M. C.; Champness, N. R.; Wilson, C. *Cryst. Eng. Comm.* **2005**, *7*, 621.

32. Pan, L.; Huang, X.; Phan, H. L. N.; Emge, T. J.; Li, J.; Wang, X. *Inorg. Chem.* **2004**, *43*, 6878.

33. Diskin-Posner, Y.; Patra, G. K.; Goldberg, I. *J. Chem. Soc. Dalton. Trans.* **2001**, 2775.

34. Pan, L.; Kelly, S.; Huang, X.; Li, J. *Chem. Commun.* **2002**, 2334.

35. Ohmura, T.; Usuki, A.; Fukumori, K.; Ohta, T.; Ito, M.; Tatsumi, K. *Inorg. Chem.* **2006**, *45*, 7988.

36. Lin, K. J. *Angew. Chem. Int. Ed.* **1999**, *38*, 2730.

37. George, S.; Goldberg, I. *Acta. Cryst.* **2005**, *E61*, m1441.

38. Deiters, E.; Bulach, V.; Hosseini, M. W. *Chem. Commun.* **2005**, 3906.

39. Hagrman, D.; Hagrman, P. J.; Zubieta, J. *Angew. Chem. Int. Ed.* **1999**, *38*, 3165.

40. Kitagawa, S.; Noro, S.-I.; Nakamura, T. *Chem Commun* **2006**, 701.

CHAPTER 3

MPF-3: AN INTERDIGITATED PORPHYRIN FRAMEWORK WITH GUEST SELECTIVE PROPERTIES

3.1 Introduction

A major driving force behind the intensive research efforts in metal-organic frameworks (MOFs) is their unique structural characteristics, which are not easily achievable in conventional solid-state materials.[1] One advantage of MOFs is their use in the rational design of a framework consisting of two kinds of building units: metal nodes and organic linkers.[1] Metal nodes are connected by organic linkers, and together they can form a remarkable variety of MOFs.[1-6] The MOF topologies are often determined by the coordination geometry of the metal nodes and the shape of the organic linkers.[1-6]

A recent addition to MOF compounds is flexible frameworks that can respond to external stimuli, such as pressure, temperature, and guest removal/uptake.[7-10] Application of external stimuli causes the framework to modify its shape while preserving the original connectivity. Kitagawa recently classified flexible MOFs into six categories.[7b] Some MOFs are flexible due to their framework topology.[7,9,10] For example, Férey and co-workers have demonstrated a three-dimensional (3D) framework that swells to 170% of its initial volume due to guest inclusion. Such a drastic change is made possible by the flexible trinuclear metal node incorporated in the framework.[9] Another example is a

MOF synthesized by Kitagawa et al., which has a two dimensional (2D) interdigitated structure whose "gate pressure" varies depending on the gas being introduced.[10]

Of the numerous organic building blocks used for MOF synthesis, we and others are particularly interested in rigid porphyrin-based ligands.[11-14] The porphyrin unit is useful because it is a metalloligand that represents an additional approach to control the structure of a MOF.[14] In this present paper, we report a flexible, interdigitated, 2D porphyrin framework MPF-3 (MPF=metalloporphyrin framework), assembled from meso-tetra(3-pyridyl)porphine (hereafter, 3-TPyP) (see Figure 3.1).

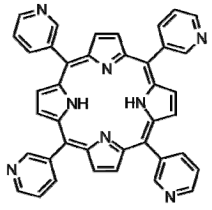

Figure 3.1. The molecular building block, meso-tetra(3-pyridyl)-porphine (3-TPyP).

3.2 Experimental Methods

3.2.1 General Methods

All chemicals were purchased from commercial sources. Crystallization experiments were performed in a Yamato DKN400 mechanical convection oven. No special precautions were taken to exclude oxygen or moisture during crystallization. Thermal gravimetric analysis (TGA) was conducted on a Perkin-Elmer STA 6000. X-ray powder diffraction data were obtained using a Rigaku D/Max-B X-ray diffractometer with Bragg-Brentano parafocusing geometry, a diffracted beam monochromator, and a conventional copper-target X-ray tube set to 40 kV and 30 mA.

Single-crystal structure determination was performed as follows: a plate-shaped crystal was sealed in a capillary tube for measurement. Geometry and intensity data were obtained at room temperature with a Bruker SMART Apex CCD area detector diffractometer. Preliminary lattice parameters and orientation matrices were obtained from three sets of frames. Data were collected using graphite-monochromated and MonoCap-collimated Mo KR radiation (λ = 0.71073 Å) by the ω-scan method.[15] Data were processed with the SAINT+ program[16] for data reduction and cell refinement. Multiscan absorption corrections were applied to the data set using the SADABS program for the area detector.[17] The structure was solved by a direct method and refined using SHELXTL.[18] Crystallographic data are summarized in Table 1.[19]

3.2.2 Synthesis

$Zn(NO_3)_2 \cdot 6H_2O$ (6.0 mg, 0.02 mmol), meso-tetra-(3-pyridyl)porphine (3-TPyP; 6.2 mg, 0.01 mmol), and *N*,*N*-dimethylformamide (DMF, 4 mL) were combined in a small capped vial. The vial contents were mixed by sonication. The purple solution was heated to 100 °C for 25 h, and then slowly cooled to room temperature over 35 h. The sample was characterized by X-ray powder diffraction and found to consist of a single phase. Yield: 36% based on porphyrin. Elemental analysis for $C_{40}H_{24}N_8Zn$. Calcd C: 70.4%, H: 3.6%, N: 16.4%; Found: C: 69.7%, H: 3.7%, N: 16.3%.

Table 3.1. Single-Crystal Data for MPF-3

Compound	MPF-3
formula	$C_{40}H_{24}N_8O_2Zn \cdot 2(C_3H_7NO)$
temperature	100 K
crystal system	monoclinic
space group	*C* 2/*c*
crystal color	red
a (Å)	29.931(5)
b (Å)	9.5639(14)
c (Å)	14.227(2)
B (deg)	109.978(2)
V (Å^3)	3827.4(10)
Z	4
ρ_{calc} (g/cm^3)	1.437
R_1 (I > 2σ (I))	0.0433
wR_2 (all reflections)	0.0887
GOF	1.055

3.2.3 Desolvation and Resolvation

The sample was centrifuged and the majority of the solvent was decanted using a pipette. The sample was heated to 150 °C for 10 h. The desolvated sample was immersed in 3 mL of various solvents and stored for 3 days.

3.3 Results and Discussion

3.3.1 Structural Description

The MPF-3 structure is shown in Figure 3.2. The porphyrin unit is axially connected through the Zn metal center. Only two of the four available pyridyl arms of each porphyrin connect to neighboring porphyrins, resulting in a 2D porphyrinic layer, as shown in Figure 3.3a. The views down the [010] and [001] directions are shown in Figure 3.3, panels b and c, respectively. The uncoordinated pyridyl arms can be seen in these two views. Uncoordinated pyridyl rings are spaced 7.1 Å apart (centroid-to-centroid distance) and are aligned parallel to each other (Figure 3.3b). Interestingly, the spacing and alignment of the uncoordinated pyridyl arms give the pyridyl arms in adjacent layers

sufficient room to interdigitate, as shown in Figure 3.4.[20] The centroid-to-centroid distance observed between the 2D layers of MPF-3 (4.0 Å or 4.4 Å due to the uneven separation of the interdigitated pyridyl arms) is beyond the traditionally accepted maximum distance for π-π interactions (3.6-3.8 Å).[21] The perpendicular separation between pyridyl arms is 3.4 or 3.7 Å due to the uneven separation of the interdigitated pyridyl arms, and the slippage distance between centroids is 2.2 Å (Figure 3.5). The perpendicular separation distance of MPF-3 (3.4 or 3.7 Å) has been previously observed, but the slippage distance of MPF-3 (2.2 Å) is larger than that of other known pyridyl systems, making the aromatic π-π interactions much weaker.[21b] However, the distance between the uncoordinated pyridyl position nitrogen (N3) of one layer and a beta hydrogen on the porphyrin of the adjacent layer (H7) is ca. 2.5 Å and is within accepted limits of a $CH_3\cdots N$ interaction.[22]

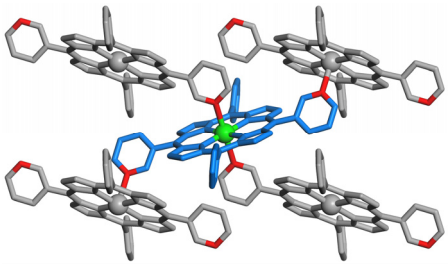

Figure 3.2. Coordination environment around the Zn metal center in MPF-3.

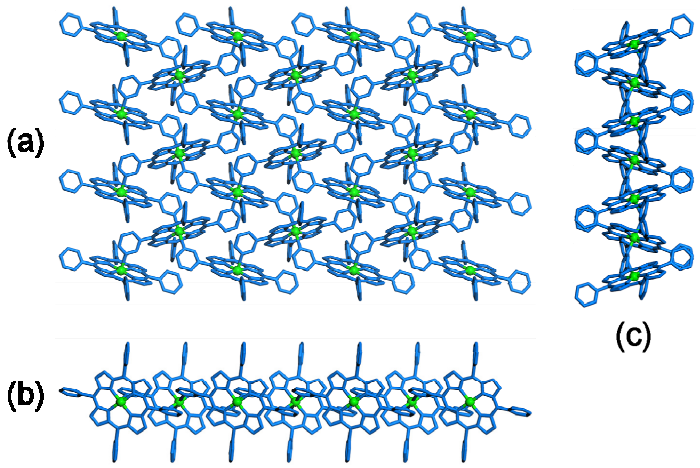

Figure 3.3. Crystal structure of MPF-3 (a) 2D layer, and views along the (b) [010] and (c) [001] directions

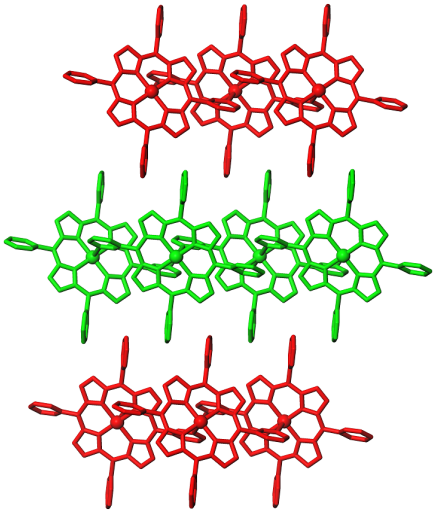

Figure 3.4. Interdigitation and stacking pattern of MPF-3.

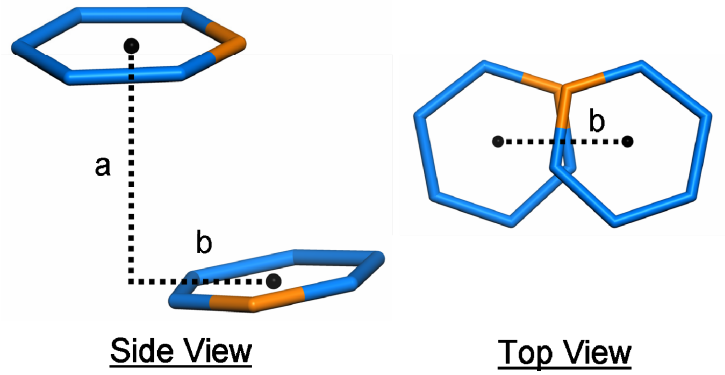

Figure 3.5. The perpendicular separation (a), and the slippage distance (b) between the pyridyl arms of MPF-3.

3.3.2 2D Tessellations

To analyze the tessellation of MPF-3, it is useful to compare MPF-3 with a similar 2D porphyrin framework, FeTPyP (TPyP=meso-tetra(4-pyridyl)porphine) reported by Li and co-workers.[23] This framework is assembled from TPyP with an octahedral Fe metal center, exhibiting stacked 2D layers.[23] A significant structural difference between MPF-3 and FeTPyP stems from the porphyrin building block: the N atoms in the pyridyl ring are in different positions.

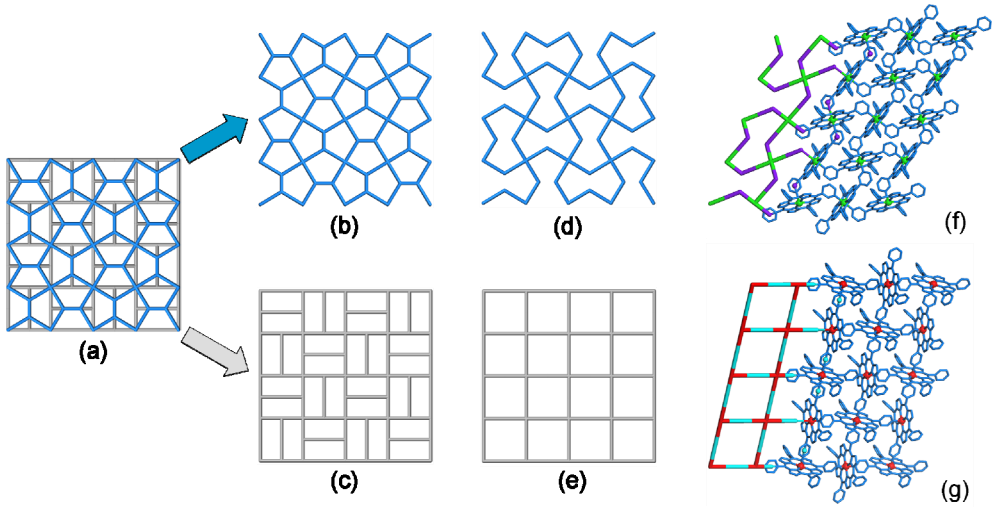

Figure 3.6. (a) Overlay of Cairo pentagonal and basketweave tessellations. Transformation of (b) Cairo pentagonal and (c) basketweave tessellations to (d) hourglass and (e) square-grid tessellations, respectively. The latter two patterns can be compared with the topologies of (f) MPF-3 (this work) and (g) the FeTPyP structure.[23]

The topologies of the FeTPyP structure and MPF-3 are analyzed by identifying the tessellation of the respective 2D layers (Figure 3.5). The relationship between MPF-3 and the FeTPyP structure can be traced to the 2D tessellations, referred to as Cairo pentagonal and basketweave tessellations, respectively.[24,25] Both tessellations are based on 3- and 4-connected nodes and have been proven to be topologically equivalent.[25] To illustrate the similarity, the Cairo pentagonal and basketweave tessellations are overlapped in Figure 3.5a. The former pattern (blue, Figure 3.5b) can be converted into the latter pattern (gray, Figure 3.5c) by bending the trigonal 3-connected nodes into T-shaped linkages while maintaining the individual connections. To relate these tessellations to MPF-3 and the FeTPyP structure, the two tessellations are modified by deleting linkages at the 3-connected nodes while leaving the overall topology unaltered (Figure 3.5d,e). The Cairo pentagonal pattern can be modified to resemble an hourglass tessellation (Figure 3.5d), which has recently been observed in MOFs by Férey and others.[26] The resulting tessellation is very similar to MPF-3 (Figure 3.5f). The metal nodes (green) and organic nodes (purple) in the center of the coordinated pyridyl rings can be connected to form a slightly distorted hourglass tessellation. Similarly, the modified basketweave tessellation becomes a square-grid tessellation (Figure 3.5e) and can be related to the FeTPyP structure (Figure 3.5g). The metal nodes of the TPyP building units and a node located in

the coordinated pyridyl arms are connected to form a square grid tessellation. Such a square-grid tessellation, known as a 2D (4,4) net, is commonly observed in MOFs.[27]

3.3.3 Framework Flexibility

Figure 3.6 shows that one-dimensional (1D) channels are sandwiched between the interdigitated layers of MPF-3. Single-crystal data revealed that these channels are filled with DMF molecules.[19] These solvent molecules play a significant role in the formation of the MPF-3 phase because we note that the MPF-3 phase does not form without DMF. Many experiments were conducted using various solvents and solvent ratios. No combination of solvents or solvent ratios that excluded DMF produced MPF-3 crystal. We hypothesize that the DMF molecule may act as a template in the formation of the framework, as has been noted in previous studies on other MOF syntheses.[28]

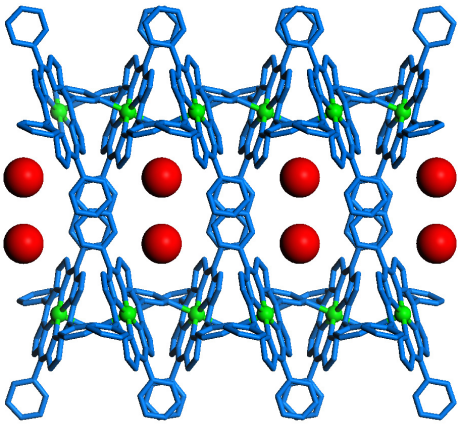

Figure 3.7. Two interdigitated layers of MPF-3 with 1D solvent channels. The red spheres indicate DMF molecules.

The interactions between the 2D layers and the guest molecules could affect the interlayer spacing. Since the reflections corresponding to the 2D interlayer spacing are often the most intense, X-ray powder diffraction can be used to monitor the interlayer

spacing of the 2D layered materials.

Testing of the flexibility of MPF-3 involves analyzing samples of the compounds at three stages: an as-synthesized sample, a desolvated sample, and a resolvated sample in various solvents. Figure 3.8 shows the powder patterns of MPF-3 in these three stages, along with the theoretical pattern from the single-crystal data. The synthesized MPF-3 has a preferential orientation that arises from diffractions from the stacked 2D layers. When the powder patterns of the synthesized sample and the desolvated sample are compared (Figure 3.8), the most intense peaks are shifted, indicating a clear change in the interlayer spacing, which decreases from 14.06 Å in the fully solvated sample to 12.41 Å in the desolvated phase. The powder pattern for the resolvated sample closely matches that for the synthesized sample, demonstrating that the structure of MPF-3 can be restored. MPF-3 was further analyzed by TGA, and it exhibited thermal stability up to 450 °C (Figure 3.9). A sample of MPF-3 was heated to 400 °C and the X-ray powder pattern taken after heating was compared to the desolvated X-ray powder pattern (Figure 3.10). On the basis of this comparison, MPF-3 is structurally stable at 400 °C.

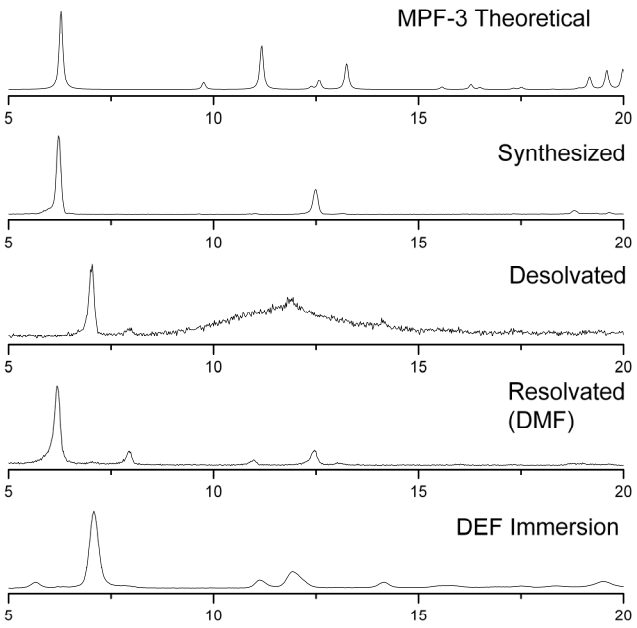

Figure 3.8. X-ray powder diffraction patterns for MPF-3.

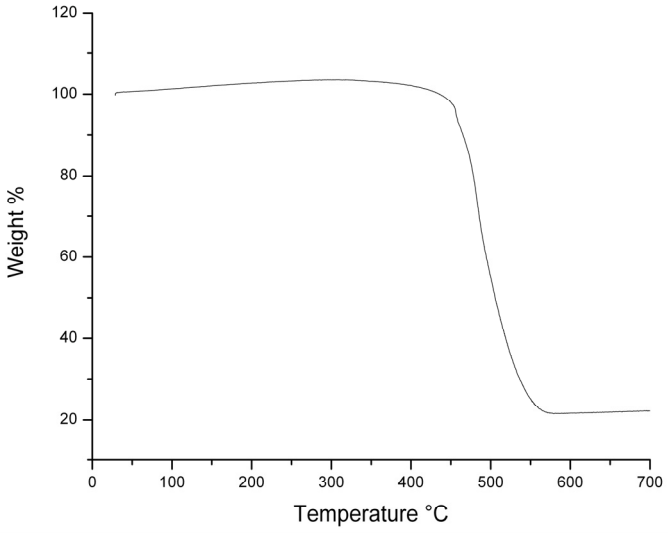

Figure 3.9. TGA for MPF-3

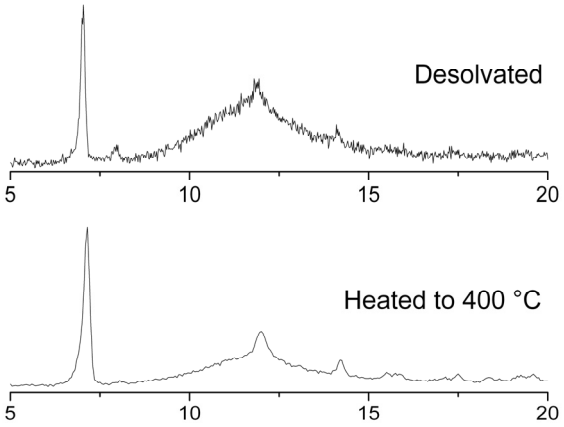

Figure 3.10. Structural stability of MPF-3 at 400 °C.

Instead of resolvating in DMF, a similar trial was run in N,N-diethylformamide (DEF). Even after immersion in DEF, the powder patterns are identical to that of the desolvated sample (Figure 3.8), indicating that the larger DEF molecules cannot be incorporated as easily as DMF molecules. Other solvents, such as hexane, yield similar results (see Appendix 1, Figure A1.1, A1.2).

The structure of the desolvated sample is unknown because of a lack of suitable crystals for X-ray single-crystal diffraction. However, changes in the interlayer spacing are evident from the X-ray powder pattern. A structural model of the desolvated phase of MPF-3 is constructed based on the single-crystal structure of the MPF-3 layer and the interlayer spacing (12.41 Å) derived from experimental X-ray powder-diffraction data for desolvated MPF-3.[29] The distance between the 2D layers is set to the interlayer spacing and the layers are moved such that they no longer interdigitate. A simulated X-ray powder diffraction pattern generated from this model shows a good match with experimental data for the desolvated phase of MPF-3 (Figure 3.11). The space group of

the structural model is monoclinic $P2_{1/a}$ with cell parameters of a = 14.227 Å, b = 9.564 Å, c = 17.105 Å, and β = 133.50°.

We hypothesize a plausible transformation mechanism of the desolvated structures (Figure 3.12). A stacking model, based on a decrease in the interlayer spacing due to movement in two directions, is sterically probable (see Appendix 1, Figure A1.3). To further support this hypothesis, Connolly surface modeling was added to the structural model of the desolvated phase of MPF-3 and the single-crystal model of the solvated phase of MPF-3 (Figure 3.13).[30] Connolly surface modeling uses a spherical probe to determine the solvent-accessible surface of a molecule or structure.[30] The probe moves around the van der Waals surface and defines a surface that bridges the gaps between neighboring atoms.[30] Additional refinement of this surface can be achieved by using a dot surface.[30] To create this surface, a dot is placed on the surface everywhere the probe does not experience van der Waals forces.[30] The probe represents a solvent molecule and the dot surface defines the areas of the molecule accessible to the solvent.[30] Figure 3.13 clearly shows that the void space of the solvated phase is drastically reduced for the desolvated phase. Solvent inclusion is unlikely in the desolvated model. The 1D channel of DMF molecules is no longer present, and the 2D layers rearrange to fill this space.

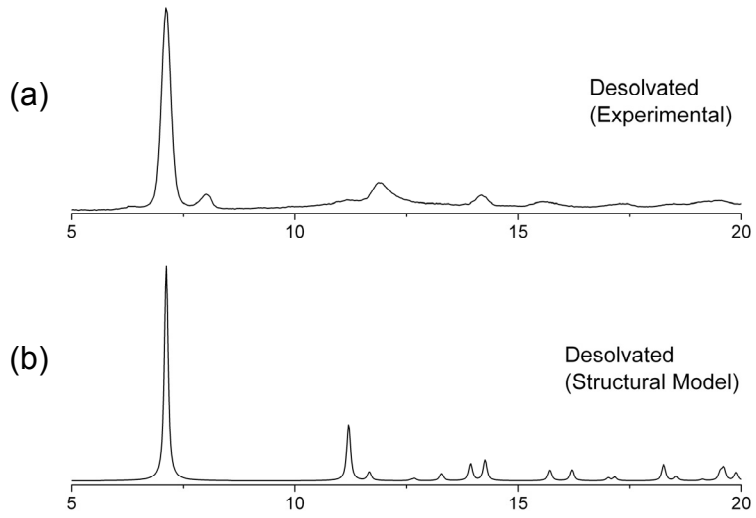

Figure 3.11. Comparison of the X-ray powder diffraction patterns of (a) the experimentally determined desolvated MPF-3 and (b) the structural model for desolvated MPF-3.

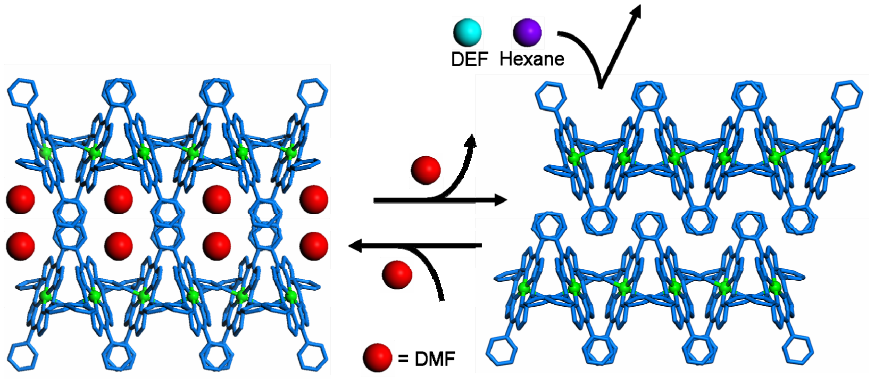

Figure 3.12. Proposed structural transition of MPF-3 and selective accommodation of DMF molecules.

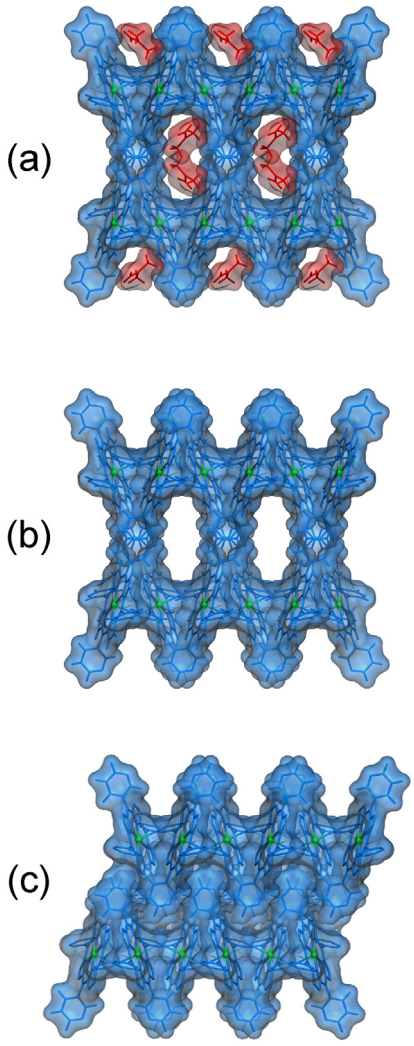

Figure 3.13. Connolly surfaces of (a) solvatedMPF-3, (b) solvatedMPF-3 with the DMF molecules removed, and (c) structural model of desolvatedMPF-3. Disorder of DMF molecules are removed for clarity.

As discussed previously, the title compound MPF-3 is similar to the FeTPyP structure. However, the 2D layer stacking shows a marked difference between MPF-3 and the FeTPyP structure. The stacking of the FeTPyP structure is quite compact (interlayer spacing of 9.15 Å) when compared to the stacking of desolvated MPF-3 (interlayer spacing of 12.41 Å), and no solvent molecules are present between the 2D layers (see Appendix 1, Figure A1.4).[23] A structure similar to FeTPyP reported by

Goldberg and co-workers uses ZnTPyP molecular building blocks and also packs more tightly than MPF-3 (interlayer spacing of 11.03 Å).[31] The flexibility of FeTPyP and ZnTPyP has not been reported yet. The 3-pyridyl connections in MPF-3 create undulating 2D layers that do not stack as tightly as the FeTPyP or ZnTPyP layers.

3.4 Conclusion

MPF-3 has been synthesized, and the topology of its framework and its guest-dependent properties are presented. When the topology of MPF-3 is analyzed, the topology of MPF-3 structure is closely related to Cairo pentagonal tessellation. The MPF-3 frameworks were exposed to several different guest molecules. X-ray powder diffraction data indicate that the movement of the 2D layers depends on the choice of guest molecule.

3.5 References

1. (a) O'Keeffe, M.; Eddaoudi, M.; Li, H.; Reineke, T.; Yaghi, O. M. *J. Solid State Chem.* **2000**, *152*, 3. (b) Delgado-Friedrichs, O.; O'Keeffe, M.; Yaghi, O. M. *Acta Cryst.* **2006**, *A62*, 350. (c) Yaghi, O. M.; O'Keeffe, M.; Ockwig, N. W.; Chae, H. K.; Eddaoudi, M.; Kim, J. *Nature* **2003**, *423*, 705. (d) Férey, G. *Chem. Soc. Rev.* **2008**, *37*, 191. (e) Kepert, C. J. *Chem. Commun.* **2006**, 695. (f) Kitagawa, S.; Kitaura, R.; Noro, S. *Angew. Chem. Int. Ed.* **2004**, *43*, 2334. (g) O'Keeffe, M. *Chem. Soc. Rev.* **2009**, *38*, 1215.
2. (a) Rowsell, J. L. C.; Yaghi, O. M. *Angew. Chem. Int. Ed.* **2005**, *44*, 4670. (b) Dincă, M.; Long, J. R. *Angew. Chem. Int. Ed.* **2008**, *47*, 6766. (c) Collins, D. J.;

Zhou, H.-C. *J. Mater. Chem.* **2007**, *17*, 3154. (d) Férey, G.; Mellot-Draznieks, C.; Serre, C.; Millange, F.; Dutour, J.; Surblé, S.; Margiolaki, I. *Science*, **2005**, *309*, 2040. (e) Rosi, N. L.; Eckert, J.; Eddaoudi, M.; Vodak, T.; Kim, J.; O'Keeffe, M.; Yaghi, O. M. *Science* **2003**, *300*, 1127. (f) Chen, B.; Zhao, X.; Putkham, A.; Hong, K.; Lobkovsky, E. B.; Hurtado, E. J.; Fletcher, A. J.; Thomas, K. M. *J. Am. Chem. Soc.* **2008**, *130*, 6411.

3. Seo, J. S.; Whang, D.; Lee, H.; Jun, S. I.; Oh, J.; Jeon, Y. J.; Kim, K. *Nature* **2000**, *404*, 982.
4. (a) Li, H.; Eddaoudi, M.; O'Keeffe, M.; Yaghi, O. M. *Nature* **1999**, *402*, 276. (b) Rowsell, J. L. C.; Eckert, J.; Yaghi, O. M. *J. Am. Chem. Soc.* **2005**, *127*, 14904.
5. (a) Liu, Y.; Eubank, J. F.; Cairns, A. J.; Eckert, J.; Kravtsov, V. C.; Luebke, R.; Eddaoudi, M. *Angew. Chem. Int. Ed.* **2007**, *46*, 3278. (b) Surblé, S.; Serre, C.; Mellot-Draznieks, C.; Millange, F.; Férey, G. *Chem. Commun.* **2006**, 284. (c) Ma, S.; Wang, X.-S.; Manis, E. S.; Collier, C. D.; Zhou, H.-C. *Inorg. Chem.* **2004**, *46*, 3432. (d) Barthelet, K.; Riou, D.; Férey, G. *Chem. Commun.* **2002**, 1492.
6. Kitagawa, S.; Noro, S.; Nakamura, T. *Chem. Commun.* **2006**, 701.
7. For reviews on flexible frameworks, see: (a) Fletcher, A. J.; Thomas, K. M.; Rosseinsky, M. J. *J. Solid State Chem.* **2005**, *178*, 2491. (b) Kitagawa, S.; Uemura, K. *Chem. Soc. Rev.* **2005**, *34*, 109. (c) Uemura, K.; Matsuda, R.; Kitagawa, S. *J. Solid State Chem.* **2005**, *178*, 2420.
8. (a) Shimomura, S.; Horike, S.; Matsuda, R.; Kitagawa, S. *J. Am. Chem. Soc.* **2007**, *129*, 10990. (b) Cussen, E. J.; Claridge, J. B.; Rosseinsky, M. J.; Kepert, C. J. *J. Am. Chem. Soc.* **2002**, *124*, 9574. (c) Kubota, Y.; Takata, M.; Matsuda, R.;

Kitaura, R.; Kitagawa, S.; Kobayashi, T. C. *Angew. Chem. Int. Ed.* **2006**, *45*, 4932. (d) Ma, S. Q.; Sun, D. F.; Wang, X. S.; Zhou, H. C. *Angew. Chem. Int. Ed.* **2007**, *46*, 2458. (e) Fletcher, A. J.; Cussen, E. J.; Bradshaw, D.; Rosseinsky, M. J.; Thomas, K. M. *J. Am. Chem. Soc.* **2004**, *126*, 9750. (f) Kondo, A.; Noguchi, H.; Carlucci, L.; Proserpio, D. M.; Ciani, G.; Kajiro, H.; Ohba, T.; Kanoh, H.; Kaneko, K. *J. Am. Chem. Soc.* **2007**, *129*, 12362. (g) Kitaura, R.; Seki, K.; Akiyama, G.; Kitagawa, S. *Angew. Chem. Int. Ed.* **2003**, *42*, 428. (h) Horike, S.; Tanaka, D.; Nakagawa, K.; Kitagawa, S. *Chem. Commun.* **2007**, 3395. (i) Llewellyn, P. L.; Bourrelly, S.; Serre, C.; Filinchuk, Y.; Férey, G. *Angew. Chem. Int. Ed.* **2006**, *45*, 7751. (j) Chen, B. L.; Ma, S. Q.; Zapata, F.; Fronczek, F. R.; Lobkovsky, E. B.; Zhou, H. C. *Inorg. Chem.* **2007**, *46*, 1233. (k) Maji, T. K.; Matsuda, R.; Kitagawa, S. *Nat. Mater.* **2007**, *6*, 142. (l) Ohba, M.; Kaneko, W.; Kitagawa, S.; Maeda, T.; Mito, M. *J. Am. Chem. Soc.* **2008**, *130*, 4475. (m) Dybtsev, D. N.; Chun, H.; Kim, K. *Angew. Chem. Int. Ed.* **2004**, *43*, 5033.

9. Serre, C.; Mellot-Draznieks, C.; Surble, S.; Audebrand, N.; Filinchuk, Y.; Férey, G. *Science* **2007**, *315*, 1828.
10. Tanaka, D.; Nakagawa, K.; Higuchi, M.; Horike, S.; Kubota, Y.; Kobayashi, L. C.; Takata, M.; Kitagawa, S. *Angew. Chem. Int. Ed.* **2008**, *47*, 3914.
11. For reviews on porphyrinic solids, see: (a) Goldberg, I. *CrystEngComm* **2008**, *10*, 637. (b) Chou, J.-H.; Kosal, M. E.; Nalwa, H. S.; Rakow, N. A.; Suslick, K. S. In *Porphyrin Handbook*; Kadish, K.; Smith, K.; Guilard, R., Eds.; Academic Press: New York, **2000**, vol. 6, 43. (c) Suslick, K. S.; Bhyrappa, P.; Chou, J. H.; Kosal, M. E.; Nakagaki, S.; Smithenry, D. W.; Wilson, S. R. *Acc. Chem. Res.* **2005**, *38*,

283. (d) Drain, C. M.; Goldberg, I.; Sylvain, I.; Falber, A. *Top. Curr. Chem.* **2005**, *245*, 55. (e) Goldberg, I. *Chem. Commun.* **2005**, 1243. (f) DeVries, L. D.; Choe, W. *J. Chem. Crystallogr*. **2009**, *39*, 229.

12. (a) Carlucci, L.; Ciani, G.; Proserpio, D. M.; Porta, F. *Angew. Chem. Int. Ed.* **2003**, *42*, 317. (b) Carlucci, L.; Ciani, G.; Proserpio, D. M.; Porta, F. *CrystEngComm* **2005**, *7*, 78. (c) Danilovic, D.; Lin, C. L.; Yuen, T.; Pan, L.; Li, J. *J. Appl. Phys.* **2007**, *101*, 09E103. (d) Ohmura, T.; Usuki, A.; Fukumori, K.; Ohta, T.; Ito, M.; Tatsumi, K. *Inorg. Chem.* **2006**, *45*, 7988. (e) Sharma, C. V. K.; Broker, G. A.; Huddleston, J. G.; Baldwin, J. W.; Metzger, R. M.; Rogers, R. D. *J. Am. Chem. Soc.* **1999**, *121*, 1137. (f) Sun, D.; Tham, F. S.; Reed, C. A.; Boyd, P. D. W. *Proc. Natl. Acad. Sci. U. S. A.* **2002**, *99*, 5088.
13. (a) The hourglass tessellation is also seen in a 3-TPyP framework reported by Goldberg, et al. See: Vinodu, M.; Goldberg, I. *CrystEngComm* **2005**, *7*, 133. (b) Alessio, E.; Geremia, S.; Mestroni, S.; Srnova, I.; Slouf, M.; Gianferrara, T.; Prodi, A. *Inorg. Chem.* **1999**, *38*, 2527.
14. (a) Choi, E.-Y.; Barron, P. M.; Novotny, R. W.; Hu, C.; Kwon, Y.-U.; Choe, W. *CrystEngComm* **2008**, *10*, 824. (b) Choi, E.-Y.; Wray, C. A.; Hu, C.; Choe, W. *CrystEngComm* **2009**, *11*, 553. (c) Barron, P. M; Son, H.-T.; Hu, C.; Choe. W. *Cryst. Growth Des*. **2009**, *9*, 1960. (d) Choi, E.-Y.; Barron, P. M.; Novotny, R. W.; Son, H.-T.; Hu, C.; Choe, W. *Inorg. Chem.* **2009**, *48*, 426. (e) Verduzco, J. M.; Chung, H.; Hu, C.; Choe, W. *Inorg. Chem.* **2009**, *48*, 9060.
15. SMART (version 6.532). *Program for Bruker CCD X-ray Diffractometer Control*, Bruker AXS Inc., Madison, WI, **2005**.

16. SAINT+ (version 6.45). *Program for Reduction of Data Collected on Bruker CCD Area Detector Diffractometer*, Bruker AXS Inc., Madison, WI, **2003**.

17. Sheldrick, G. M. SADABS, version 2.10, *Program for Empirical Absorption Correction of Area Detector Data*, University of Göttingen, **2007**.

18. Sheldrick, G. M. SHELXTL, version 6.14, *Program Package for Structure Solution and Refinement*, Bruker Analytical X-ray Systems, Inc., Madison, WI, **2003**.

19. Crystallographic data for MPF-3 has been deposited at the Cambridge Crystallographic Data Center as supplementary publications (CCDC: 660983 for MPF-3). The data can be obtained free of charge at www.ccdc.cam.ac.uk/conts/retrieving.html (or from the CCDC, 12 Union Road, Cambridge CB2 1EZ, UK; fax: +441223336033; e-mail: deposit@ccdc.cam.ac.uk).

20. For examples of interdigitated MOFs, see Zou, Y.; Hong, S.; Park, M.; Chun, H.; Lah, M. S. *Chem. Commun*. **2007**, 5182.

21. (a) Janiak, C. *Dalton Trans.* **2000**, 3885. (b) Hohenstein, E. G.; Sherrill, C. D. *J. Phys. Chem.* **2009**, *113*, 878. (c) Reger, D. L.; Debreczeni, A.; Reinecke, B.; Rassolov, V.; Smith, M. D. *Inorg. Chem.* **2009**, *48*, 8911. (d) The interaction energy for a perpendicular separation distance of 3.5 Å and a slippage distance of 1.4 Å was calculated to be -2.78 kcal mol^{-1} for a pyridine dimer system [$(Py)_2$ P2a(+)] similar to the overlapping pyridyl arms of MPF-3.[21b] A potential energy curve was also calculated for a range of slippage distances and a fixed perpendicular separation distance of 3.5 Å.[21b] Based on this curve, a reasonable

estimation of the possible interaction energy of the pyridyl arms of MPF-3 was estimated to be -2.0 kcal mol^{-1}.

22. (a) Kobrsi, I.; Knox, J. E.; Heeg, M. J.; Schlegel, H. B.; Winter, C. H. *Inorg. Chem.* **2005**, *44*, 4894. (b) Xu, J.; Wang, W.-L.; Lin, T.; Sun. Z.; Lai, Y.-H. *Supramol. Chem.* **2008**, *20*, 723.

23. Pan, L.; Kelly, S.; Huang, X. Y.; Li, J. *Chem. Commun.* **2002**, 2334.

24. (a) Cairo pentagonal tessellation is a simple 2D tiling by congruent pentagons with a symmetry of *p4gm*.[25] The dual of this tessellation is (3^2.4.3.4) net, which is an Archimedean tiling. (b) Cairo pentagonal tessellation can be seen in paintings such as *Shells and Starfish* by M. C. Escher. See: http://www.mcescher.com (c) For examples of Cairo pentagonal tessellation in MOFs, see refs. 24d and 24e. (d) Moulton, B.; Lu, J. J.; Zaworotko, M. J. *J. Am. Chem. Soc.* **2001**, *123*, 9224. (e) Thakuria, R.; Sarma, B.; Nangia, A. *Cryst. Growth Des*. **2008**, *8*, 1471.

25. (a) Lockwood, E. H.; Macmillan, R. H., *Geometric Symmetry*. Cambridge University Press: Cambridge; New York, **1978**; p 89. (b) Pearce, P.; Pearce, S., *Polyhedra Primer*. Van Nostrand Reinhold: New York, **1978**; p 35. (c) Grünbaum, B.; Shephard, G. C., *Tilings and Patterns*. W.H. Freeman: New York, **1987**; p 172. (d) O'Keeffe, M.; Hyde, B. G., *Crystal Structures I. Patterns and Symmetry*, Mineralogical Society of America, Washington DC, **1996**; p 207.

26. For examples of hourglass tessellation found in other MOFs, see: (a) Dybtsev, D. N.; Yutkin, M. P.; Peresypkina, E. V.; Virovets, A. V.; Serre, C.; Férey, G. ; Fedin, V. P. *Inorg. Chem.* **2007**, *46*, 6843. (b) Liu, Z.; Liu, P.; Chen, Y.; Wang, J.; Huang, M. H. *Inorg. Chem. Commun*. **2005**, *8*, 212.

27. Ohrstrom, L.; Larsson, K. *Molecule-Based Materials*, *The Structural Network Approach*; Elsevier B.V.: Amsterdam, The Netherlands, **2005**.

28. (a) Fang, Q. R.; Zhu, G. S.; Xue, M.; Wang, Z. P.; Sun, J. Y.; Qiu, S. L. *Cryst. Growth Des.* **2008**, *8*, 319. (b) Burrows, A. D.; Cassar, K.; Friend, R. M. W.; Mahon, M. F.; Rigby, S. P.; Warren, J. E. *CrystEngComm* **2005**, *7*, 548. (c) Choi, E. Y.; Park, K.; Yang, C. M.; Kim, H.; Son, J. H.; Lee, S. W.; Lee, Y. H.; Min, D.; Kwon, Y. U. *Chem. Eur. J.* **2004**, *10*, 5535.

29. The structural model of the desolvated phase of MPF-3 was constructed using Materials Studio. Materials Studio (version 4.3.0.0). *Program for Molecular Modeling and Analysis*, *Accelrys Software Inc.*, **2008**.

30. Connolly, M. L. *Science* **1983**, *221*, 709.

31. Recently, Goldberg and coworkers reported a new 2D ZnTPyP structure. In this structure, dichlorobenzene molecules reside between the 2D layers. See: Koner, R.; Goldberg, I. *Acta Cryst. C* **2009**, *65*, m139.

CHAPTER 4

E-MOF-1: AN EXPANDABLE PORPHYRIN FRAMEWORK WITH $CdSO_4$-TYPE TOPOLOGY

4.1 Introduction

A new class of metal-organic frameworks (MOFs), flexible MOFs, have also been the subject of significant study recently,.[1-4] These flexible MOFs respond to external stimuli, such as pressure, temperature, and guest removal/uptake and change their structures while preserving original connectivity .[1-4] Flexible frameworks that are thermally responsive have been shown to have the potential to also be negative thermal expansion (NTE) materials.[5b,5c] Such NTE materials decrease in volume as the temperature increases, and are relatively rare.[6] The importance of NTE materials is their use in creating composites that can be engineered to "match" a desired thermal expansion behavior.[5a] The NTE material is often combined with a material with an appropriate positive thermal expansion (PTE) material.[5a] Such composites with nearly zero thermal expansion can be used in many applications, including refractive index compensation for optics, biomedical devices that expand with bone or teeth, and sensitive circuit boards.[5a,5d] Optical components with such a coating would provide protection against the loss of ideal optical properties as the temperature varied.[5a] MOFs that have demonstrated NTE include derivatives of IRMOF-1[5c,5d], and $Ag_3[Co(CN)_6]$, a MOF with "colossal" NTE .[7]

In this present paper, we report a flexible, 3D porphyrin framework E-MOF-1 (E-MOF = Expandable Metal-Organic Framework), assembled from meso-tetra(4-pyridyl)porphine (hereafter, 4-TPyP) (see Figure 4.1) and cadmium atoms that form a $CdSO_4$ topology (**cds**).[8-15] E-MOF-1 is subjected to thermal testing and demonstrates anisotropic thermal-expansion behavior.[7]

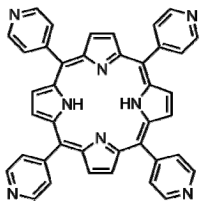

Figure 4.1. The molecular building block, meso-tetra(4-pyridyl)porphine (4-TPyP).

4.2 Experimental Methods

4.2.1 General Methods

All chemicals were purchased from commercial sources. Crystallization experiments were performed in a Yamato DKN400 mechanical convection oven. No special precautions were taken to exclude oxygen or moisture during crystallization. X-ray powder diffraction data were obtained using a Rigaku D/Max-B X-ray diffractometer with Bragg–Brentano parafocusing geometry, a diffracted beam monochromator, and a conventional copper-target X-ray tube set to 40 kV and 30 mA. Temperature-dependent X-ray data was obtained through two sources: Bruker SMART Apex CCD area detector diffractometer and the 11-BM beamline located at Argonne National Labs.[16] Single-crystal structure determination was performed as follows. A plate-shaped crystal was sealed in a capillary tube for measurement. Geometry and intensity data were obtained at

room temperature with a Bruker SMART Apex CCD area detector diffractometer. Preliminary lattice parameters and orientation matrices were obtained from three sets of frames. Data were collected using graphite monochromated and MonoCap-collimated Mo K_α radiation (λ = 0.71073 Å) by the ω scan method.[17] Data were processed with the SAINT+ program[18] for data reduction and cell refinement. Multiscan absorption corrections were applied to the data set using the SADABS program for the area detector.[19] The structure was solved by a direct method and refined using SHELXTL.[20]

4.2.2 Synthesis

Meso-tetra(4-pyridyl)porphine (4-TPyP; 5.7mg, 0.009 mmol), 1,1,2,2-tetrachloroethane (TCE, 0.75 mL) , and methanol (MeOH, 0.25 mL) were added to a long tube. 3'-chloroaniline (1 mL) is layered on next and CdI_2 (7.2 mg, 0.02 mmol) and *N*,*N'*-dimethylacetamide (DMA, 1 mL) are layered on last. The tube opening was wrapped with parafilm and allowed to sit undisturbed at room temperature for several months.

4.2.3 Temperature Dependent Powder Diffraction

Temperature-dependent X-ray powder-diffraction scans were conducted on E-MOF-1 at temperatures below and above room temperature (297K). Single-crystal data were taken at 100K, 200K, and 297K. Synchrotron data (11-BM beamline, Argonne National Labs) were also taken with a range of 297K-495K. The temperature was increased in 25K increments from 297-375K, and then increased to 425K, 475K, and 495K. The temperature was cycled back to room temperature between each elevated temperature scan, and a room temperature scan was conducted. This made for a total of 6

elevated scans, and 8 room temperature scans. Adding in the single-crystal scan, a total of 17 temperature scans were collected on E-MOF-1.

4.3 Structural description

Figure 4.2 shows the single-crystal structure of E-MOF-1, a metal-organic framework formed of 4-TPyP units linked to cadmium atoms through coordination to the pyridyl groups of the porphyrin. Each cadmium atom is equatorially coordinated to four porphyrins, and is capped with two iodide atoms axially in a nearly ideal octahedral geometry. Closer examination of the structure of E-MOF-1 reveals that the framework has a $CdSO_4$ (**cds**) topology. This type of (4,4) net is often reported for MOFs.[10] Many of the previously reported MOFs are interpenetrated.[11-13] This is not surprising because the **cds** net is self-dual.[11] The frameworks have demonstrated 2- to 5-fold interpenetration.[11,12] E-MOF-1 is a rare example of a MOF with **cds** topology that is not interpenetrated.[13]

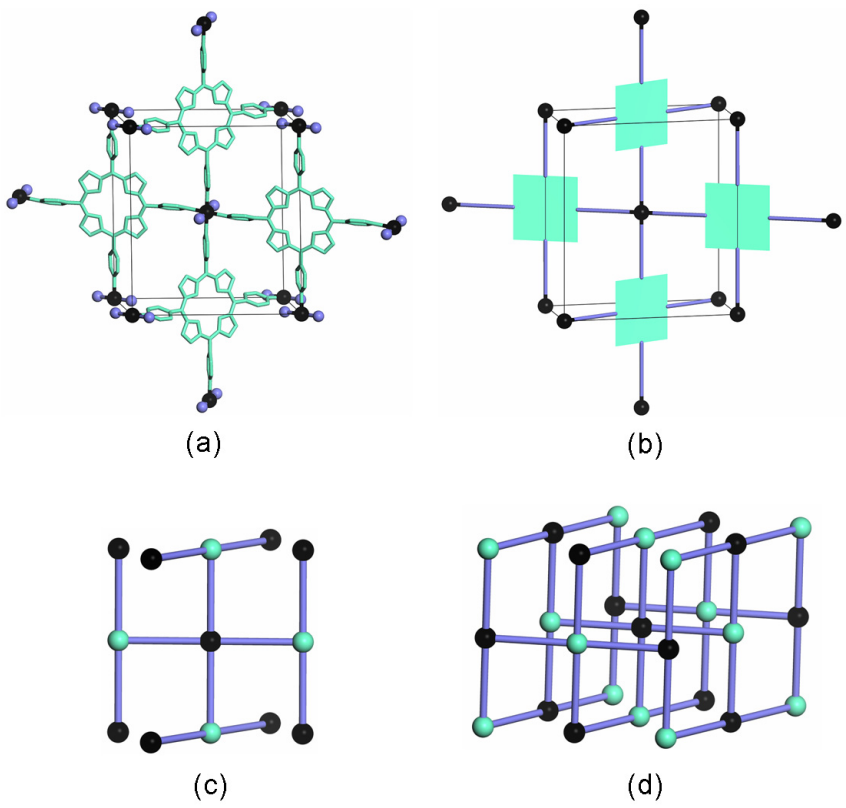

Figure 4.2. The (a) unit cell of E-MOF-1 is shown and can be simplified by (b) removing the iodide ions and replacing the porphyrins with squares that also have D_{4h} symmetry. Further simplification can be achieved by (c) replacing each porphyrin square with a 4-connected node centered in the pore of the porphyrin. The unit cell can then be seen as the (d) 4-connected net **cds**.

4.4 Topological Analysis

As shown in Figure 4.3, the **cds** topology can be derived from the primitive cubic structure and is related to another 4-connected net **nbo**. The **cds** net is derived from the primitive cubic structure by deleting half of all the connections that are perpendicular to a (001) plane. In this way the **cds** net retains all of the connection nodes of the primitive cubic structure, but has significantly fewer connections than the primitive-cubic type (see Figure 4.3). The **nbo** net is created by deleting the nodes and connections at each corner

of the primitive-cubic structure, and deleting the node in the center. When we build these structural models, we discover that the rigid nature of the primitive cubic structure is maintained in the **nbo** topology, while absent in the **cds** topology. It is quite remarkable to see that the deleted connectors allow the **cds** topology to be continuously variable. The range of variability of a framework with **cds** topology is directly related to the interaction between the framework and itself. Because E-MOF-1 has the **cds** topology, we envision that E-MOF-1 could be flexible in the solid state. In order to test flexibility of E-MOF-1, we carried out a temperature-dependent X-ray diffraction study.

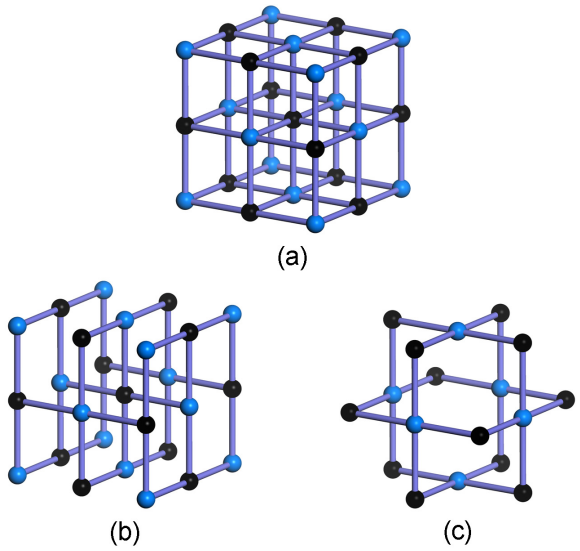

Figure 4.3. The (a) primitive-cubic structure can be related to the 4-connected nets (b) **cds** and (c) **nbo**.

4.5 Thermal Response of E-MOF-1

One of the definitions of a flexible framework includes the ability to be cycled between a "resting" state and a state in which some stress is applied (guest exchange, change in temperature, increase in pressure, etc.).[1-4] In order to test thermal flexibility, the

E-MOF-1 sample sent to Argonne National Labs was cycled between room temperature and a series of elevated temperatures to determine if it would return to its "resting" state. Temperature-dependent X-ray diffraction scans were run on two different samples. We have low temperature single-crystal data on one sample, and high temperature synchrotron powder diffraction on a different sample. The cell parameters of the single-crystal sample were taken directly from the solved structure file (Appendix 2, Table A2.1). The cell parameters of the synchrotron sample were calculated using the raw 2θ data, the indexing data of the room temperature single-crystal scan, and the program Unit Cell (For a more detailed explanation, See Appendix 2.).[21] These 17 temperature scans provided a significant amount of data on which to judge the flexibility of E-MOF-1. As shown in Figure 4.4, all scans indicate that the unit cell of E-MOF-1 changes with temperature. Figure A2.1 compares the single-crystal, room-temperature scan with the synchrotron powder diffraction room temperature scans. It can be seen that E-MOF-1 does return to its room temperature state after being heated to as high as 495K. Figure 4.5 shows the shift of two peaks with indexing (101) and (110) to lower Q values (where $Q = 2\pi/d$, and d is the d-spacing) as the temperature was increased. This supports the flexible behavior of E-MOF-1 because both peaks have indexing that corresponds to a significant change in the a and/or b parameter. The a parameter undergoes the most drastic change when the temperature is increased (see Figure 4.6). Over a 350K temperature range, the a parameter changes by nearly 6% (Figure 4.6)! In contrast, the b parameter only changes by less than 1% and the c parameter changes by less than 0.3%. Therefore, we conclude that a change in a parameter is the major factor in altering the shape of E-MOF-1 in the solid state.

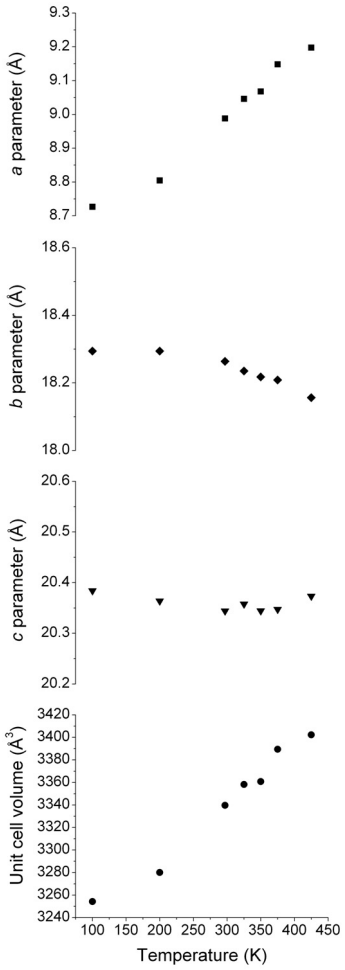

Figure 4.4. Experimental cell parameters and unit-cell volume of E-MOF-1 plotted versus temperature.

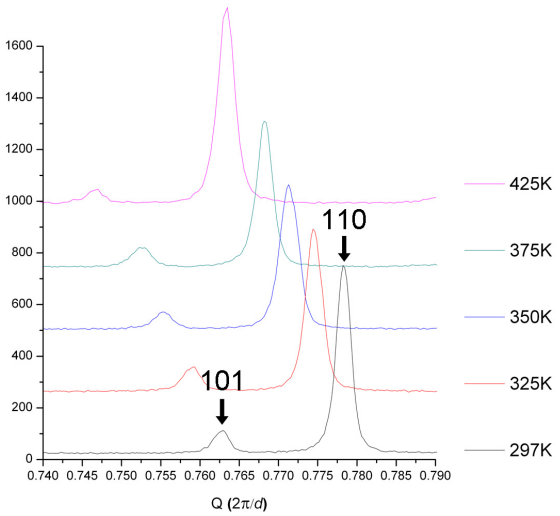

Figure 4.5. Indexed peaks (101) and (110) shifting to lower *Q* values (indicating an increase in cell parameter) as the temperature is increased.

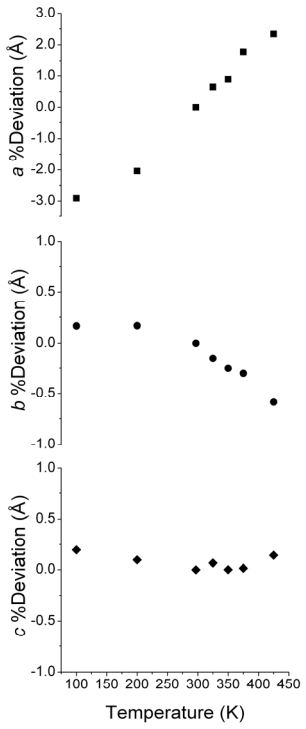

Figure 4.6. The percent deviation of each cell parameter from their respective room-temperature values are plotted versus temperature.

4.6 Flexible Model

Figure 4.7 illustrates a simple structural model of E-MOF-1 that has been created to analyze the flexibility of E-MOF-1 and its **cds** topology. When the unit cell of E-MOF-1 is viewed down the *c*-axis (Figure 4.7), it reveals that the structure deviates from the ideal **cds** topology shown in Figure 4.3. The angle 2θ is less than 90°, and this accounts for the tilted structure shown in Figure 4.2. The behavior of this angle in response to external stimulus is one of the ways in which we tested the flexibility of E-MOF-1. A change in θ will change *a* and *b* parameters of E-MOF-1 according to a simple trigometric relationship as shown in Figure 4.7. The orthorhombic space group of E-MOF-1, *Pnnm* (No. 58), allows the use of this simple model because of the way that E-MOF-1 is oriented within the unit cell (see Appendix 2, Table A2.1). The porphyrin node-to-cadmium-node distance, *d*, is defined as *c*/2. The *c* parameter is assumed to be unaffected by any change in θ, and the hypotenuse of the right-angle triangle is the same distance as the value of the *c* parameter (see Figure 4.7). This provides a way to arrive at an experimental value of θ utilizing only cell parameters derived from measured X-ray powder-diffraction data. With aid of this simple model, we are able to estimate θ from X-ray powder patterns. The flexible model can also be used to calculate a theoretical minimum value of θ (for more information see Appendix 2). Due to the close contact between the adjacent iodine anions, the theoretical minimum value of θ was calculated to be 24.55° (see the detailed calculation in Appendix 2). This is little more than 1° different from the θ value for the single-crystal structure at 100K (which is the smallest observed θ value, 25.5°). This would seem to indicate that E-MOF-1 is near its minimum θ value at 100K.

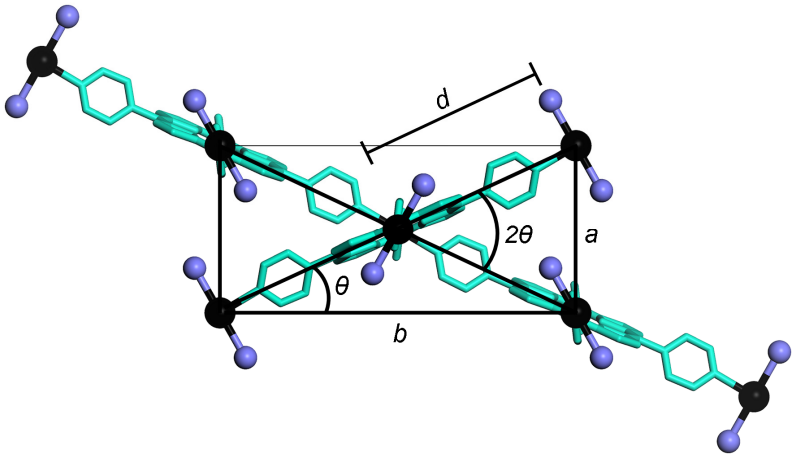

Figure 4.7. View of E-MOF-1 unit cell down the *c* direction. The cell parameters *a* and *b* are related trigometrically by the angles *2θ* and *θ*, and the porphyrin node to cadmium node distance *d*. The triangle defined by *a*, *b*, and *θ* is defined as a right angle triangle.

Before finding the *θ* values at each temperature, the flexible model was first tested. To test the reliability of the model, a theoretical curve was derived from the trigometric relationships shown in Figure 4.7 (see Appendix 2). The curve is generated from a range of *b*-parameter values that were imported to calculate theoretical *a*-parameter values. The experimental cell parameters *a* versus cell parameter *b* were then plotted on the curve. As shown in Figure 4.8, the curve (and therefore the flexible model) fits reasonably well with the experimental data. It should be noted that the points most divergent from the curve occur at higher temperatures. This indicates that at higher temperatures, the flexible model no longer applies. The flexible model is dependent on E-MOF-1 maintaining an orthorhombic space group. The divergence from the model at higher temperatures could be due to an impurity phase present at higher temperatures. This is supported by examining the powder-diffraction patterns taken at the highest

temperature (495K). Additional reflections that do not correspond to E-MOF-1 appear at 495K (see Figure A2.3).

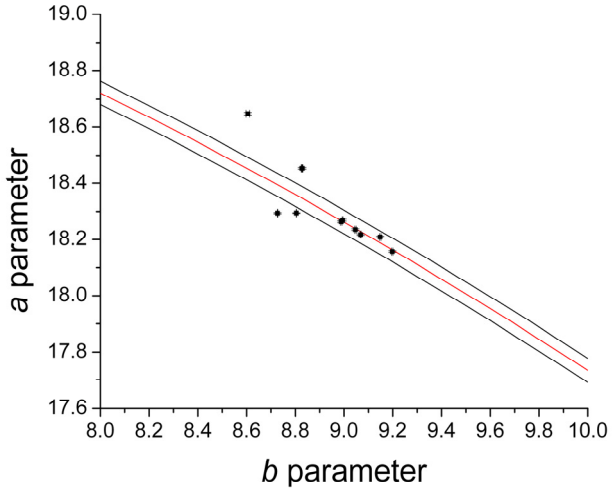

Figure 4.8. The experimental values of the *a* and *b* parameters plotted against the a theoretical curve (red) derived from the flexible model. The error bars for each point are plots of the error of the cell parameters *a* and *b*. The black curves are derived from the standard deviation of the *c* parameter (which is directly comparable to the curve as 2*d* is part of the calculation of the curve and $c = 2d$) to the theoretical curve.

The flexible model is used to calculate the θ values of E-MOF-1 at various temperatures (Figure 4.9). Simple trigometric relationships were used to remove *d* from the calculation so that only the experimental values of the *a* and *b* parameters were used to calculate the θ values at each temperature (for more information see Appendix 2). It can be seen that as the temperature increases the value of θ continues to increase in a nearly linear fashion (Figure 4.9). Perhaps more significant is that the θ value of E-MOF-1 changes by almost 2° over the entire temperature range. The accuracy of the model was again tested by comparing the calculated values of the three single-crystal θ values to the angle of θ generated by using an atomic modeling program and the solved single-crystal

files (see Table A.2.2). The largest percent deviation between the "measured" θ and the calculated θ was less than 2%. This deviation supports the viability of our flexible model.

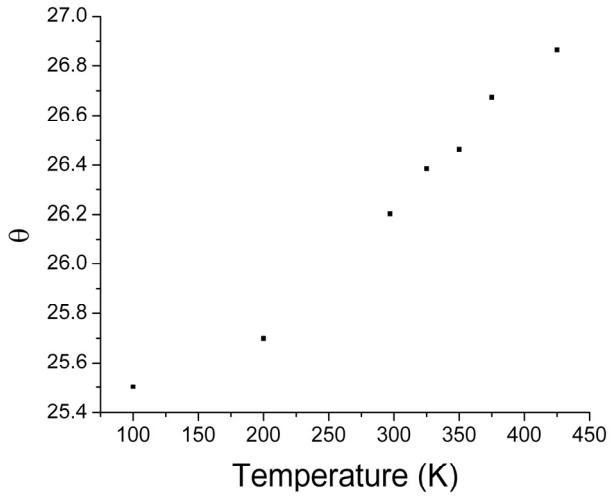

Figure 4.9. The angle, θ plotted versus temperature for the low temperature single-crystal data, initial room temperature synchrotron data, and elevated temperature synchrotron data up to 425K.

4.7 "Colossal" Thermal Expansion

Negative thermal expansion (NTE) is the property of a material that decreases in volume as the temperature is increased. These materials are useful in creating composites that contain materials with positive thermal expansion (PTE, far more common) and have tunable thermal properties.[5,6] Other applications include thermally-tuned biomedical devices, ceramics for use in sensitive electronics, and thermally stable optical materials for precise spectrographic sensing.[5,6] Specific structural characteristics are important when analyzing whether or not a material has the potential to be a NTE material. One of these characteristics is the type of bonding present in the material. Material with rigid unit nodes (RUMS) or M─O bonds are the most common canidates.[6] RUMS usually

consist of rigid polyhedral units that can change orientation in space without losing connectivity.[6] When heated, the material contracts as the RUMS rotate.[6] NTE materials with M—O bonds undergo transverse vibrations at the M—O—M linkage (the "guitar string" model) when the temperature is increased. This reduces the volume of the material as the metal atoms are pulled closer together by the vibration of the oxygen atom.[6] Additional structural features, such as linker length, can also increase the NTE properties of a material.[5c] E-MOF-1 is most like the RUM model and does not posses any M—O bonds. In E-MOF-1, the rigid polyhedral units would be the cadmium nodes between the porphyrins. E-MOF-1 does experience NTE in the *b* parameter only, and furthermore; the positive thermal expansion (PTE) in the *a* parameter is so drastic that it qualifies as "colossal" as defined by Goodwin, et *al.*[15] The anisotropic nature of E-MOF-1 is one of its more interesting properties.

To determine if a material has "colossal" ($|\alpha| \geq 100 \times 10^{-6}\ K^{-1}$) NTE, its coefficient of thermal expansion (CTE or α) must first be calculated.[15] The α-value of a material is $\alpha = \frac{\Delta \text{ cell parameter}}{\Delta \text{Temperature} \cdot \text{cell parameter}}$ (for more information, see Appendix 2). The α-value can be either positive (PTE) or negative (NTE). Some materials posses a α value that changes as the temperature is increased.[6] This usually involves a change in symmetry.[6] The temperature dependent scans did not indicate that E-MOF-1 ever changed symmetry over the temperature range tested. The calculation of the α-value of E-MOF-1 also supports the stability of its symmetry as it does not change the sign of α after the lowest temperature scan (see Appendix 2). It has also been shown that the inclusion of another framework within the primary framework (interpenetration) has an effect on the magnitude of α.[5b] The α-values of two isostructural frameworks (one with a

secondary 1D framework and one without) were calculated.[5b] The change in one of the cell parameters for the framework without a secondary framework was nearly an order of magnitude greater than the framework with the secondary framework.[5b] The largest value of α for the *a* parameter of E-MOF-1 (approximately 225 x 10^{-6} K^{-1}) is larger than any previously reported α value.[15] E-MOF-1 is not a NTE material, but there is significant NTE behavior in the *b* parameter, and a "colossal" PTE behavior in the *a* parameter. This does suggest that it may be possible for a derivative of E-MOF-1 to be used as part of a NTE/PTE composite.

4.8 Conclusion

E-MOF-1 has been synthesized, and the topology of its framework and its thermal dependent properties are presented. When the topology of E-MOF-1 is analyzed, the topology of E-MOF-1 is shown to be a match for the **cds** framework. Temperature-dependent X-ray powder and single-crystal diffraction data were collected at a wide range of temperatures. The single-crystal and synchrotron powder-diffraction data indicate that the movement of the 3D structure of E-MOF-1 is sensitive to changes in temperature. A flexible model was developed from this data and used to further analyze the behavior of E-MOF-1 as the temperature was varied. Additionally, it was discovered that E-MOF-1 posses "colossal" NTE in the *a*-parameter, demonstrating highly anisotropic thermal behavior.

4.9 References

1. For reviews on flexible frameworks, see: (a) Fletcher, A. J.; Thomas, K. M.; Rosseinsky, M. J. *J. Solid State Chem.* **2005**, *178*, 2491. (b) Kitagawa, S.; Uemura, K. *Chem. Soc. Rev.* **2005**, *34*, 109. (c) Uemura, K.; Matsuda, R.; Kitagawa, S. *J. Solid State Chem.* **2005**, *178*, 2420.
2. (a) Shimomura, S.; Horike, S.; Matsuda, R.; Kitagawa, S. *J. Am. Chem. Soc.* **2007**, *129*, 10990. (b) Cussen, E. J.; Claridge, J. B.; Rosseinsky, M. J.; Kepert, C. J. *J. Am. Chem. Soc.* **2002**, *124*, 9574. (c) Kubota, Y.; Takata, M.; Matsuda, R.; Kitaura, R.; Kitagawa, S.; Kobayashi, T. C. *Angew. Chem. Int. Ed.* **2006**, *45*, 4932. (d) Ma, S. Q.; Sun, D. F.; Wang, X. S.; Zhou, H. C. *Angew. Chem. Int. Ed.* **2007**, *46*, 2458. (e) Fletcher, A. J.; Cussen, E. J.; Bradshaw, D.; Rosseinsky, M. J.; Thomas, K. M. *J. Am. Chem. Soc.* **2004**, *126*, 9750. (f) Kondo, A.; Noguchi, H.; Carlucci, L.; Proserpio, D. M.; Ciani, G.; Kajiro, H.; Ohba, T.; Kanoh, H.; Kaneko, K. *J. Am. Chem. Soc.* **2007**, *129*, 12362. (g) Kitaura, R.; Seki, K.; Akiyama, G.; Kitagawa, S. *Angew. Chem. Int. Ed.* **2003**, *42*, 428. (h) Horike, S.; Tanaka, D.; Nakagawa, K.; Kitagawa, S. *Chem. Commun.* **2007**, 3395. (i) Llewellyn, P. L.; Bourrelly, S.; Serre, C.; Filinchuk, Y.; Férey, G. *Angew. Chem. Int. Ed.* **2006**, *45*, 7751. (j) Chen, B. L.; Ma, S. Q.; Zapata, F.; Fronczek, F. R.; Lobkovsky, E. B.; Zhou, H. C. *Inorg. Chem.* **2007**, *46*, 1233. (k) Maji, T. K.; Matsuda, R.; Kitagawa, S. *Nat. Mater.* **2007**, *6*, 142. (l) Ohba, M.; Kaneko, W.; Kitagawa, S.; Maeda, T.; Mito, M. *J. Am. Chem. Soc.* **2008**, *130*, 4475. (m) Dybtsev, D. N.; Chun, H.; Kim, K. *Angew. Chem. Int. Ed.* **2004**, *43*, 5033.

3. Serre, C.; Mellot-Draznieks, C.; Surble, S.; Audebrand, N.; Filinchuk, Y.; Férey, G. *Science* **2007**, *315*, 1828.
4. Tanaka, D.; Nakagawa, K.; Higuchi, M.; Horike, S.; Kubota, Y.; Kobayashi, L. C.; Takata, M.; Kitagawa, S. *Angew. Chem. Int. Ed.* **2008**, *47*, 3914.
5. Applications and examples of NTE materials: (a) Evans, J. S. O. *J. Chem. Soc., Dalton Trans.* **1999**, 3317. (b) Goodwin, A. L.; Kennedy, B. J.; Kepert, C. J. *J. Am. Chem. Soc.* **2009**, *131*, 6334. (c) Dubbeldam, D.; Walton, K. S.; Ellis, D. E.; Snurr, R. Q. *Angew. Chem. Int. Ed.* **2007**, *46*, 4496. (d) Han, S. S.; Goddard III, W. A. *J. Phys. Chem. C* **2007,** *111,* 15185.
6. Review on NTE: Miller, W.; Smith, C. W.; Mackenzie, D. S.; Evans, K. E. *J. Mater. Sci.* **2009**, *44*, 5441.
7. "Colossal" NTE: Goodwin, A. L.; Calleja, M.; Conterio, M. J.; Dove, M. T.; Evans, J. S. O.; Keen, D. A.; Peters, L.; Tucker, M. G. *Science* **2008**, *319*, 794.
8. For reviews on porphyrinic solids, see: (a) Goldberg, I. *CrystEngComm* **2008**, *10*, 637. (b) Chou, J.-H.; Kosal, M. E.; Nalwa, H. S.; Rakow, N. A.; Suslick, K. S. In *Porphyrin Handbook*; Kadish, K.; Smith, K.; Guilard, R., Eds.; Academic Press: New York, **2000**, vol. 6, 43. (c) Suslick, K. S.; Bhyrappa, P.; Chou, J. H.; Kosal, M. E.; Nakagaki, S.; Smithenry, D. W.; Wilson, S. R. *Acc. Chem. Res.* **2005**, *38*, 283. (d) Drain, C. M.; Goldberg, I.; Sylvain, I.; Falber, A. *Top. Curr. Chem.* **2005**, *245*, 55. (e) Goldberg, I. *Chem. Commun.* **2005**, 1243. (f) DeVries, L. D.; Choe, W. *J. Chem. Crystallogr*. **2009**, *39*, 229.
9. (a) Carlucci, L.; Ciani, G.; Proserpio, D. M.; Porta, F. *Angew. Chem. Int. Ed.* **2003**, *42*, 317. (b) Carlucci, L.; Ciani, G.; Proserpio, D. M.; Porta, F.

CrystEngComm **2005**, *7*, 78. (c) Danilovic, D.; Lin, C. L.; Yuen, T.; Pan, L.; Li, J. *J. Appl. Phys.* **2007**, *101*, 09E103. (d) Ohmura, T.; Usuki, A.; Fukumori, K.; Ohta, T.; Ito, M.; Tatsumi, K. *Inorg. Chem.* **2006**, *45*, 7988. (e) Sharma, C. V. K.; Broker, G. A.; Huddleston, J. G.; Baldwin, J. W.; Metzger, R. M.; Rogers, R. D. *J. Am. Chem. Soc.* **1999**, *121*, 1137. (f) Sun, D.; Tham, F. S.; Reed, C. A.; Boyd, P. D. W. *Proc. Natl. Acad. Sci. U. S. A.* **2002**, *99*, 5088.

10. (a) Choi, E.-Y.; Barron, P. M.; Novotny, R. W.; Hu, C.; Kwon, Y.-U.; Choe, W. *CrystEngComm* **2008**, *10*, 824. (b) Choi, E.-Y.; Wray, C. A.; Hu, C.; Choe, W. *CrystEngComm* **2009**, *11*, 553. (c) Barron, P. M; Son, H.-T.; Hu, C.; Choe. W. *Cryst. Growth Des*. **2009**, *9*, 1960. (d) Choi, E.-Y.; Barron, P. M.; Novotny, R. W.; Son, H.-T.; Hu, C.; Choe, W. *Inorg. Chem.* **2009**, *48*, 426. (e) Verduzco, J. M.; Chung, H.; Hu, C.; Choe, W. *Inorg. Chem.* **2009**, *48*, 9060.
11. Ohrstrom, L.; Larsson, K. *Molecule-Based Materials*, *The Structural Network Approach*; Elsevier B.V.: Amsterdam, The Netherlands, **2005**.
12. For 2-fold **cds** net, Shin, D. M.; Lee, I. S.; Chung, Y. K.; Lah, M. S. *Chem. Commun.* **2003,** 1036. (b) Long, D. L.; Blake, A. J.; Champness, N. R.; Schröder, M. *Chem. Commun,* **2000,** 1369.
13. For 5-fold **cds** net, see: (a) Bhogala, B. R.; Thallapally, P. K.; Nangia, A. *Cryst. Growth Des.* **2004,** *4,* 215. (c) Carlucci, L.; Ciani, G.; Proserpio, D. M.; Rizzato, S. *J. Chem. Soc., Dalton Trans.* **2000,** 3821.
14. For the structures with **cds** and other nets, see: (a) Carlucci, L.; Ciani, G.; Proserpio, D. M. *Chem. Commun.* **2004,** 380.

15. For non-interpenetrating cds net, see: (a) Sarkar, M.; Biradha, K. *Cryst. Eng. Comm.* **2004,** *6,* 310. (b) Thirumurugan, A.; Natarajan, S. *Cryst. Growth Des.* **2006,** *6,* 983.

16. http://11bm.xor.aps.anl.gov/description.html

17. SMART (version 6.532). *Program for Bruker CCD X-ray Diffractometer Control*, Bruker AXS Inc., Madison, WI, **2005**.

18. SAINT+ (version 6.45). *Program for Reduction of Data Collected on Bruker CCD Area Detector Diffractometer*, Bruker AXS Inc., Madison, WI, **2003**.

19. Sheldrick, G. M. SADABS, version 2.10, *Program for Empirical Absorption Correction of Area Detector Data*, University of Göttingen, **2007**.

20. Sheldrick, G. M. SHELXTL, version 6.14, *Program Package for Structure Solution and Refinement*, Bruker Analytical X-ray Systems, Inc., Madison, WI, **2003**.

21. Unit Cell program: Holland, T. J. B.; Redfern, S. A. T. *Mineral. Mag.* **1997**, *61*, 65.

Appendix 1

ADDITIONAL STRUCTURAL ANALYSIS DATA OF MPF-3

A1.1 Resolvation Results

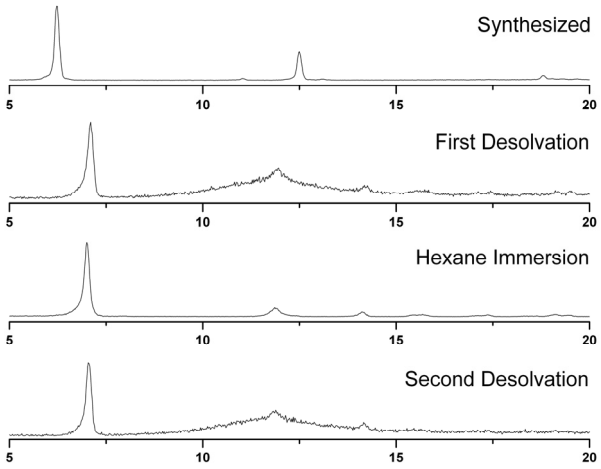

Figure A1.1. X-ray powder diffraction patterns of the desolvation and attempted hexane resolvation of MPF-3.

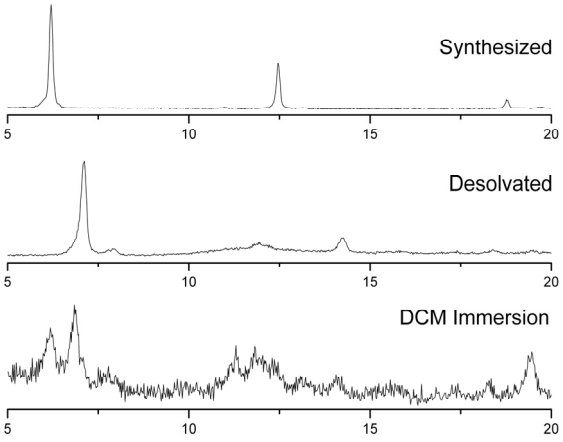

Figure A1.2. X-ray powder diffraction patterns of the desolvation and attempted DCM resolvation of MPF-3.

A1.2 Construction of the Desolvated Structural Model of MPF-3

A structural model of the desolvated phase of MPF-3 is constructed based on data from the solvated single-crystal structure and the desolvated experimental X-ray powder-diffraction pattern. In constructing the model, several assumptions were also made: the layers do not change orientation in relation to one another; the layers do not form a new structural pattern, and the layers do not lose connectivity. With these guidelines in place, the next step was to analyze the most intense peaks of both the solvated and desolvated structures. It is assumed that the metal atoms present in the periodically stacked layers of MPF-3 account for the majority of the diffraction signal observed. The 2D layers of MPF-3 can be thought of as "layers" of metal atoms separated by *d* (Bragg's Law layer spacing). Therefore, the peak shift observed in the desolvated X-ray powder-diffraction pattern would be due to a change in the layer spacing (*d*). This is important to note when analyzing the desolvated X-ray powder-diffraction pattern, and is key to adjusting the layer stacking and the desolvated cell parameters.

The stacking distance *d* can be related to the *a*-parameter, but the layers do not stack in the *a* direction. This is due to the symmetry of the unit cell. The relationship of the *a*-parameter, and, thus, the *a* direction, is as follows: $d = a \cdot \sin(180 - \beta)$. If is assumed that β is held constant, there is a direct relationship between the *a* cell parameter and the *d* spacing. Additionally, single-crystal data of the solvated phase indicates that the most intense peaks correspond to the *h00* reflections. These assumptions and relationships were the basis used to construct the desolvated structural model.

A blank crystal lattice was first constructed using the space group of the solvated phase and altering the *a* parameter based on the experimental X-ray powder-diffraction

pattern and the relationship between *a* and *d* detailed above. The theoretical *d* spacing of the desolvated sample was calculated using the most intense peak position of the experimental X-ray powder diffraction pattern and Bragg's Law. The *a*-parameter of the new unit cell was set to this value. All other cell parameters were left unchanged from the solvated single-crystal data. Once the crystal lattice was constructed, the two layers from the solvated single-crystal model were transplanted into the new unit cell. The layer separation was then adjusted to the theoretical *d* spacing (12.41 Å). The layers were moved within the cell to the proper separation distance. This process was repeated until 16 layers were constructed. This process was necessary to provide a large enough sample of the periodicity of the model for Materials Studio to find the symmetry of the desolvated structural model. A simulated X-ray powder-diffraction pattern generated from this model matches well with experimental data for the desolvated phase of MPF-3 (see Figure S8). The space group for the structural model is monoclinic $P2_1/a$ with the cell parameters of a = 14.227 Å, b = 9.564 Å, c = 17.105 Å, and β = 133.50°.

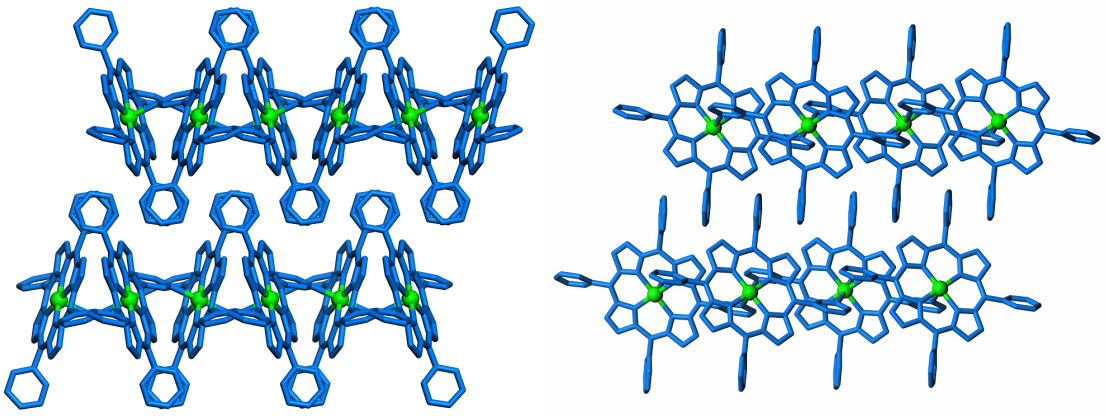

Figure A1.3. A structural model for the desolvated of MPF-3 showing the stacking pattern (left) and the interdigitated layers (right).

Table A1.1. Unit cell parameters and atomic parameters of the structural model for desolvated MPF-3.

MPF-3			
Monoclinic P$2_1/a$ a = 14.227 Å, b = 9.564 Å, c = 17.105 Å, β = 133.498°			
atom	x	y	z
N1	0.29948	0.02679	0.86533
C2	0.10318	0.05779	0.69134
N3	0.45724	0.90700	0.07985
C4	0.33800	0.89070	0.04601
C5	0.35501	0.83900	0.13480
C6	0.48438	0.82400	0.22037
C7	0.54806	0.86780	0.18564
C8	0.07812	0.99949	0.74745
C9	0.20184	0.98079	0.85702
C10	0.21815	0.92270	0.94148
C11	0.09879	0.88890	0.91864
C12	0.07851	0.75380	0.93514
C13	0.00462	0.98889	0.88244
N14	0.97817	0.71963	0.92184
C15	0.89778	0.95322	0.86477
C16	0.88808	0.81723	0.88594
N17	0.08132	0.13439	0.43454
C18	0.30858	0.12729	0.73778
C19	0.24232	0.07339	0.76548
C20	0.22788	0.18208	0.62551
C21	0.15572	0.09289	0.53663
C22	0.22093	0.32408	0.60445
C23	0.14473	0.36998	0.49982
C24	0.07678	0.27298	0.41840
H25	0.33653	0.47702	0.44400
H26	0.22177	0.90241	0.32631
H27	0.36078	0.98630	0.51749
H28	0.48625	0.81573	0.66691
Zn29	0.50000	0.00000	0.00000

A1.3 Stacking Patterns of MPF-3 and the FeTPyP Structure

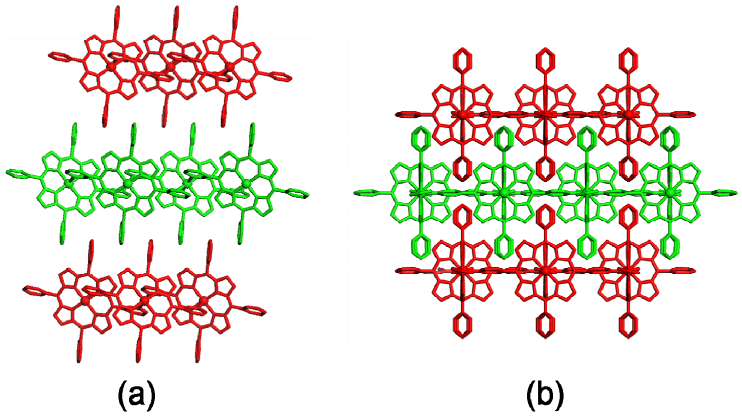

Figure A1.4. Interdigitation and stacking pattern of (a) MPF-3 and (b) FeTPyP.

Appendix 2
CALCULATIONS FOR THE CELL PARAMETERS, FLEXIBLE MODEL, AND COEFFICIENT OF THERMAL EXPANSION

A2.1 Cell Parameters Derived from Synchrotron Data

The raw 2θ data form Argonne was converted to d-spacing values. The resulting data was plotted and the peaks were compared to the indexed d-spacing peaks of the room-temperature single-crystal data. The experimental synchrotron peak position and peak intensity were compared to the peak positions and the corresponding F^2 values of the single-crystal data. This method was used to index the major experimental peaks of each temperature-dependent data set. These peaks were then analyzed for peaks that were present in all of the scans. The scans contained 13 peaks that were common to the scans from 197K to 425K. The peak indexing and position of each peak were used to calculate the cell parameters of for each temperature run. The program Unit Cell was used to generate the cell parameters of the temperature-dependent experimental data.[1] The cell parameters were used to analyze the temperature-dependent nature of E-MOF-1. The significant cell parameter and volume change of E-MOF-1 indicates that E-MOF-1 is a flexible framework. The cell parameters change at different temperatures, and then return to nearly the same room temperature (297K) values.

Table A2.1. Single-crystal Data for E-MOF-1

formula	$C_{58}H_{52}CdCl_2I_2N_{12}O_2$
temperature	297 K
crystal system	orthorhombic
spacegroup	*Pnnm*
crystal color	dark red
a (Å)	8.9939(17)
b (Å)	18.270(4)
c (Å)	20.380(4)
V (Å^3)	3348.7(11)
Z	2
ρ_{calc} (g/cm^3)	1.375
R_1 (I > 2σ (I))	0.0426
wR_2 (all reflections)	0.1182
GOF	1.01

Table A2.2. Temperature Dependent Cell Parameter Data

SINGLE CRYSTAL							
Temperature (K)	Parameters				% Deviation		
	a	b	c		a	b	c
100	8.7268(10)	18.294(2)	20.384(2)		-2.9079	0.1658	0.1957
200	8.8045(6)	18.2945(13)	20.3640(15)		-2.0435	0.1680	0.0969
297	8.9939(17)	18.270(4)	20.380(4)		0.0638	0.0311	0.1736
ELEVATED TEMPERATURE							
Temperature (K)	Parameters				% Deviation		
	a	b	c		a	b	c
297	8.9882	18.2638	20.3443		0.0000	0.0000	0.0000
325	9.0463	18.2354	20.3578		0.6467	-0.1557	0.0664
350	9.0680	18.2177	20.3445		0.8883	-0.2526	0.0011
375	9.1483	18.2089	20.3474		1.7817	-0.3010	0.0152
425	9.1979	18.1565	20.3733		2.3332	-0.5874	0.1428
475	8.6052	18.6475	20.1989		-4.2614	2.1009	-0.7145
495	8.8266	18.4536	20.1426		-1.7973	1.0392	-0.9915

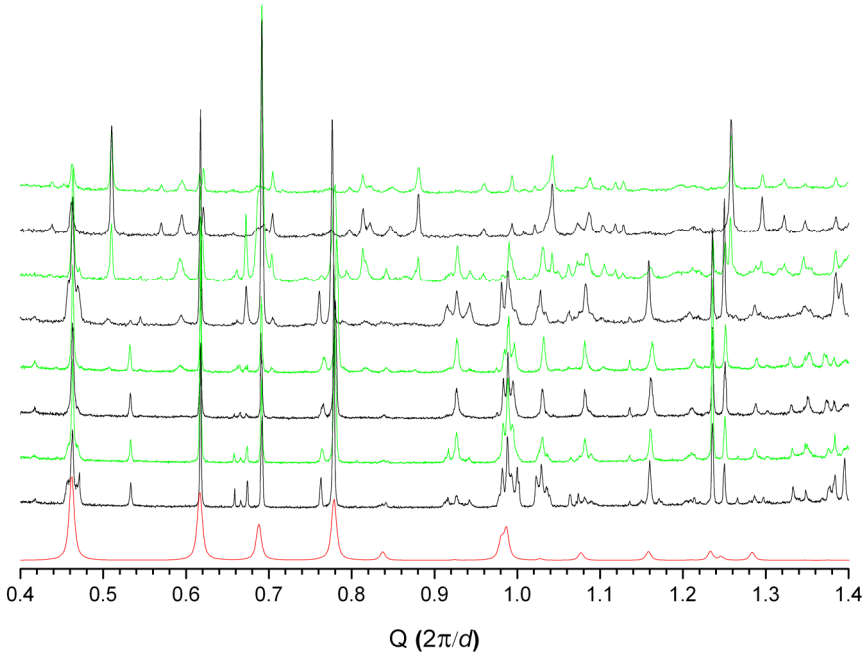

Figure A2.1. The room-temperature single-crystal data (red) and room-temperature synchrotron powder diffraction data plotted as *Q*.

A2.2 Flexible Model Calculations and Relationships

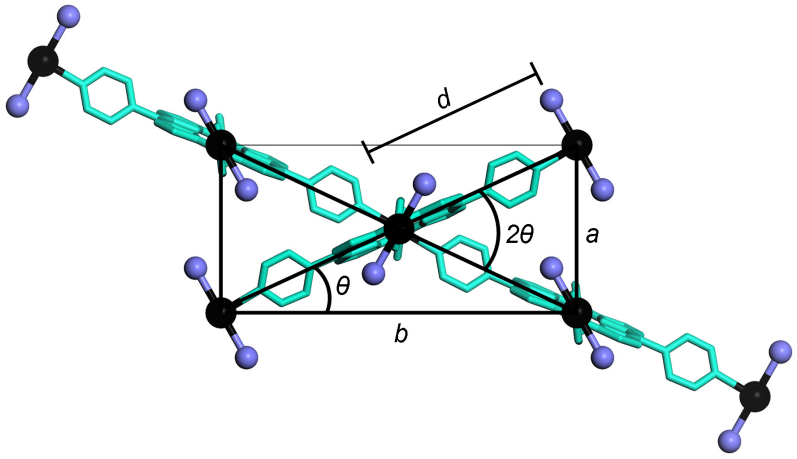

Figure A2.2. Flexible model of E-MOF-1.

Trigometric relationships:

Eqn-A2.1 $a = 2d \sin\theta$

Eqn-A2.2 $b = 2d \cos\theta$

Eqn-A2.3 $c = 2d$

Eqn-A2.4 $a^2 = 4d^2 \sin^2\theta$

Eqn-A2.5 $b^2 = 4d^2 \cos^2\theta$

Factor Eqn-A2.4 and Eqn-A2.4 using the trigometric relationship: $\sin^2\theta + \cos^2\theta = 1$

$$a^2 + b^2 = 4d^2$$

Eqn-A2.6 $a = \sqrt{4d^2 - b^2}$

Calculating Theta

Calculate theta using only experimental values using Pythagorean Theorem and previously defined trigometric relationships

Eqn-A2.7 $a^2 + b^2 = c^2$, where $c = 2d$

Eqn-A2.8 $2d = \sqrt{a^2 + b^2}$

Substitute Eqn-A2.8 into Eqn-A2.1

Eqn-A2.9 $a = \left(\sqrt{a^2 + b^2}\right)\sin\theta$

Rearrange Eqn-A2.9 and solve for Theta

Eqn-A2.10 $\sin\theta = \dfrac{a}{\sqrt{a^2 + b^2}}$

Table A2.3. Comparison of Theta from the Model and Single-crystal Data

Single Crystal Temperature	Measured θ	Calculated θ	% Deviation
100	25.502	25.107	1.548
200	25.700	25.486	0.833
297	26.211	26.151	0.228

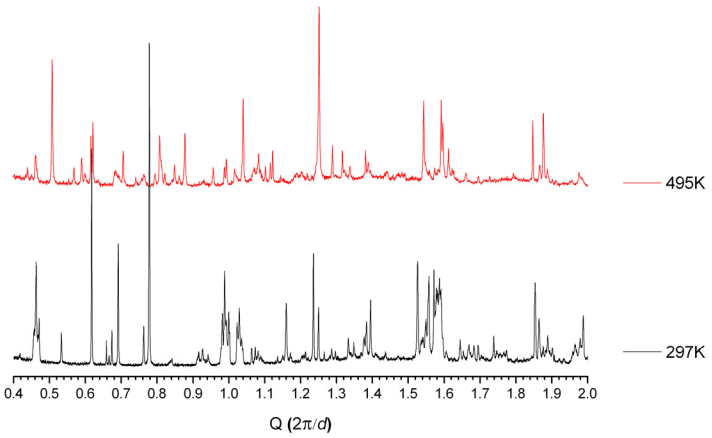

Figure A2.3. At higher temperatures, previously unobserved peaks appear in the powder-diffraction pattern of E-MOF-1 and some peaks disappear completely.

A2.3 Calculation of the Minimum Value of θ

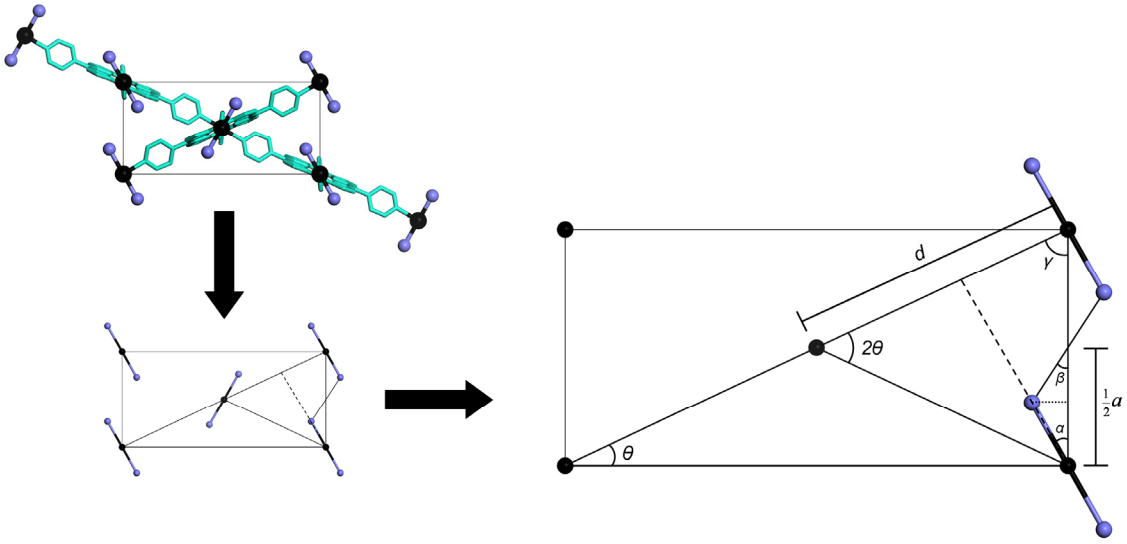

Figure A2.4. Model of E-MOF-1 viewed down the c direction defining the trigometric relationships of theoretical iodide interactions where *a* is the *a*-parameter and γ, α, and β are angles. All triangles are defined as right-angle triangles.

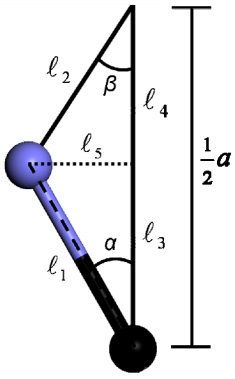

Figure A2.5. Expanded view of the trigometric relationships of theoretical iodide interactions where ℓ_n is a length.

Trigonometric relationships

$2\theta + 2\gamma = 180$

$\gamma = 90 - \theta$

$\alpha + \gamma + 90 = 180$

$\alpha + (90 - \theta) + 90 = 180$

$\alpha - \theta = 0$

Constants:

$d = 10.182$

$\ell_1 = 2.935$

$\ell_2 = 1.98$

Eqn-A2.12 $\therefore \alpha = \theta$

$\ell_3 = \ell_1 \cos\alpha$

$\ell_4 = \ell_2 \cos\beta$

Eqn-A2.13 $\ell_3 + \ell_4 = 1/2a$

Eqn-A2.14 $1/2a = \ell_1 \cos\alpha + \ell_2 \cos\beta$

Eqn-A2.15 $\ell_1 \sin\alpha = \ell_2 \sin\beta = \ell_5$

Eqn- A2.16 $\ell_1^2 \sin^2\alpha = \ell_2^2 \sin^2\beta$

Do not have a relationship defining β, and so it must be factored out.

Eqn- A2.17 $\sin^2\beta + \cos^2\beta = 1$

Eqn- A2.18 $\sin^2\beta = 1 - \cos^2\beta$

Substitute for $\sin^2\beta$

Eqn- A2.19 $\ell_2^2(1 - \cos^2\beta) = \ell_1^2 \sin^2\alpha$

Eqn- A2.20 $1 - \cos^2\beta = \left(\frac{\ell_1}{\ell_2}\right)^2 \sin^2\alpha$

Eqn- A2.21 $-\cos^2\beta = \left(\frac{\ell_1}{\ell_2}\right)^2 \sin^2\alpha - 1$

Eqn- A2.22 $\ell_2^2(\cos^2\beta) = (1 - \left(\frac{\ell_1}{\ell_2}\right)^2 \sin^2\alpha)\ell_2^2$

Eqn- A2.23 $\ell_2^2 \cos^2\beta = \ell_2^2 - \ell_1^2 \sin^2\alpha$

Remove β term using Eqn- A2.23.

$1/2a = \ell_1 \cos\alpha + \ell_2 \cos\beta$

$\ell_2 \cos\beta = 1/2a - \ell_1 \cos\alpha$

$(\ell_2 \cos\beta)^2 = (1/2a - \ell_1 \cos\alpha)^2$

$(\ell_2 \cos\beta)^2 = (1/2a - \ell_1 \cos\alpha)(1/2a - \ell_1 \cos\alpha)$

$(\ell_2 \cos\beta)^2 = 1/4a^2 - 1/2a\ell_1 \cos\alpha - 1/2a\ell_1 \cos\alpha - \ell_1^2 \cos^2\alpha$

Eqn- A2.24 $(\ell_2 \cos\beta)^2 = 1/4a^2 - a\ell_1 \cos\alpha - \ell_1^2 \cos^2\alpha$

Substitute Eqn-24 into Eqn-23.

Eqn- A2.25 $1/4a^2 - a\ell_1 \cos\alpha - \ell_1^2 \cos^2\alpha = \ell_2^2 - \ell_1^2 \sin^2\alpha$

Simplify terms by converting sines to cosines.

Eqn- A2.26 $\ell_2^2 - \ell_1^2 \sin^2\alpha = \ell_2^2 - \ell_1^2 - \ell_1^2 \cos^2\alpha$

Substitute Eqn-25 into Eqn-24 and use relationship of Eqn-12.

Eqn- A2.27 $1/4a^2 - a\ell_1 \cos\theta - \ell_1^2 \cos^2\theta = \ell_2^2 - \ell_1^2 - \ell_1^2 \cos^2\theta$

$1/4a^2 - a\ell_1 \cos\theta = \ell_2^2 - \ell_1^2$

Eqn- A2.28 $1/4a^2 - a\ell_1 \cos\theta - \ell_2^2 + \ell_1^2 = 0$

Define *a*.

Eqn- A2.29 $a = 2d \sin\theta$

Substitute Eqn- A2.29 into Eqn- A2.28.

$1/4(2d \sin\theta)^2 - (2d \sin\theta)\ell_1 \cos\theta - \ell_2^2 + \ell_1^2 = 0$

Eqn- A2.30 $d^2 \sin^2\theta - 2d \sin\theta\ell_1 \cos\theta - \ell_2^2 + \ell_1^2 = 0$

Simplification

$d^2 \sin^2\theta - \ell_2^2 + \ell_1^2 = 2d \sin\theta\ell_1 \cos\theta$

Eqn- A2.31 $d^2 \sin^2\theta + \ell_1^2 - \ell_2^2 = \ell_1 2d \sin\theta\cos\theta$

Everything in terms of sine

$(d^2 \sin^2\theta + (\ell_1^2 - \ell_2^2))^2 = (\ell_1 2d \sin\theta\cos\theta)^2$

$d^4 \sin^4\theta + d^2 \sin^2\theta(\ell_1^2 - \ell_2^2) + d^2 \sin^2\theta(\ell_1^2 - \ell_2^2) + (\ell_1^2 - \ell_2^2)^2 = \ell_1^2 4d^2 \sin^2\theta(1 - \sin^2\theta)$

Eqn- A2.32

$$d^4 \sin^4\theta + 2d^2 \sin^2\theta(\ell_1^2 - \ell_2^2) + (\ell_1^2 - \ell_2^2)^2 = 4d^2\ell_1^2 \sin^2\theta - 4d^2\ell_1^2 \sin^4\theta$$

Simplification

$$d^4 \sin^4\theta + 2d^2 \sin^2\theta(\ell_1^2 - \ell_2^2) + (\ell_1^2 - \ell_2^2)^2 - \ell_1^2 4d^2 \sin^2\theta + \ell_1^2 4d^2 \sin^4\theta = 0$$

$$d^4 \sin^4\theta + 4d^2\ell_1^2 \sin^4\theta + 2d^2\ell_1^2 \sin^2\theta - 2d^2\ell_2^2 \sin^2\theta - 4d^2\ell_1^2 \sin^2\theta + (\ell_1^2 - \ell_2^2)^2 = 0$$

$$d^4 \sin^4\theta + 4d^2\ell_1^2 \sin^4\theta - 2d^2\ell_2^2 \sin^2\theta - 2d^2\ell_1^2 \sin^2\theta + (\ell_1^2 - \ell_2^2)^2 = 0$$

Eqn- A2.33 $$\sin^4\theta(d^4 + 4d^2\ell_1^2) - \sin^2\theta(2d^2\ell_2^2 + 2d^2\ell_1^2) + (\ell_1^2 - \ell_2^2)^2 = 0$$

Substitute the term $(\sin^2\theta = x)$ into Eqn-33

Eqn- A2.34 $$x^2(d^4 + 4d^2\ell_1^2) - x(2d^2\ell_2^2 + 2d^2\ell_1^2) + (\ell_1^2 - \ell_2^2)^2 = 0$$

Substitute constants into Eqn- A2.34

$$14320.37x^2 - 2599.01x + 22.032 = 0$$

Solve for x where $x = \text{minimum angle of E - MOF - 1 (framework at most "relaxed" state)}$

$\boxed{\theta = 24.55°}$

A2.4 Coefficient of Thermal Expansion (α)

The coefficient of thermal expansion was calculated to determine if the thermal behavior of E-MOF-1 (a change of nearly 6% in the *a*-parameter) was large enough to be noteworthy. The coefficient of thermal expansion (CTE or α) was calculated by first plotting the cell parameter data versus temperature. The best polynomial fit was found and the first derivative was taken of this function. The CTE at each temperature was then calculated by first substituting temperature values into the first derivative function of the polynomial fit (*x*) to find the slope at that temperature. The slope was then divided by the cell parameter value at that temperature to arrive at the CTE.

Coefficient of Thermal Expansion: $\alpha = \dfrac{\Delta \text{ cell parameter}}{\Delta \text{Temperature} \cdot \text{cell parameter}}$

Where $\dfrac{\Delta \text{ cell parameter}}{\Delta \text{Temperature}} = \text{first derivative of the polynomial fit} = \text{slope of polynomial fit}$

Table A2.4. Colossal positive thermal expansion of the *a* parameter

a parameter				
Temperature (K)	TERM 1 ($-0.00297 + 3.40316 \times 10^{-5}x$)	TERM 2 ($-5.7984 \times 10^{-8}x^2$)	SLOPE	α ($10^{-6}K^{-1}$)
100	4.3316E-04	-5.7984E-04	-1.4668E-04	-16.81
200	3.8363E-03	-2.3194E-03	1.5170E-03	172.29
297	7.1374E-03	-5.1147E-03	2.0227E-03	224.89
297	7.1374E-03	-5.1147E-03	2.0227E-03	225.04
325	8.0903E-03	-6.1246E-03	1.9657E-03	217.29
350	8.9411E-03	-7.1030E-03	1.8380E-03	202.69
375	9.7919E-03	-8.1540E-03	1.6379E-03	179.03
425	1.1493E-02	-1.0473E-02	1.0201E-03	110.90
475	1.3195E-02	-1.3083E-02	1.1237E-04	13.06
495	1.3876E-02	-1.4208E-02	-3.3189E-04	-37.60

Table A2.5. Negative thermal expansion of the *b* parameter

b parameter			
Temperature (K)	Term 1 ($5.55322 \times 10^{-4} + -3.73264 \times 10^{-6}x$)	SLOPE	α ($10^{-6}K^{-1}$)
100	1.7996E-04	1.7996E-04	9.84
200	-1.9331E-04	-1.9331E-04	-10.57
297	-5.5537E-04	-5.5537E-04	-30.40
297	-5.5537E-04	-5.5537E-04	-30.41
325	-6.5989E-04	-6.5989E-04	-36.19
350	-7.5320E-04	-7.5320E-04	-41.34
375	-8.4652E-04	-8.4652E-04	-46.49
425	-1.0332E-03	-1.0332E-03	-56.90
475	-1.2198E-03	-1.2198E-03	-65.41
495	-1.2944E-03	-1.2944E-03	-70.15

Table A2.6. Positive thermal expansion of the *c* parameter

c parameter			
Temperature (K)	Term 1 ($-6.11871 \times 10^{-04} + 2.09198 \times 10^{-06}x$)	SLOPE	α ($10^{-6}K^{-1}$)
100	-4.0267E-04	-4.0267E-04	-19.75
200	-1.9348E-04	-1.9348E-04	-9.50
297	9.4471E-06	9.4471E-06	0.46
297	9.4471E-06	9.4471E-06	0.46
325	6.8022E-05	6.8022E-05	3.34
350	1.2032E-04	1.2032E-04	5.91
375	1.7262E-04	1.7262E-04	8.48
425	2.7722E-04	2.7722E-04	13.61
475	3.8182E-04	3.8182E-04	18.90
495	4.2366E-04	4.2366E-04	21.03

A2.5 References

1. Unit Cell program: Holland, T. J. B.; Redfern, S. A. T. *Mineral. Mag.* **1997**, *61*, 65.